Atmospheric
Chemistry
and Physics

OMI tropospheric NO$_2$ profiles from cloud slicing: constraints on surface emissions, convective transport and lightning NO$_x$

M. Belmonte Rivas[1,2], P. Veefkind[1,2], H. Eskes[2], and P. Levelt[1,2]

[1]Technical University of Delft, Delft, the Netherlands
[2]Royal Netherlands Meteorology Institute, De Bilt, the Netherlands

Correspondence to: M. Belmonte Rivas (belmonte@knmi.nl)

Abstract. We derive annual and seasonal global climatologies of tropospheric NO$_2$ profiles from OMI cloudy observations for the year 2006 using the cloud-slicing method on six pressure levels centered at about 280, 380, 500, 620, 720 and 820 hPa. A comparison between OMI and the TM4 model tropospheric NO$_2$ profiles reveals striking overall similarities, which confer great confidence to the cloud-slicing approach to provide details that pertain to annual as well as seasonal means, along with localized discrepancies that seem to probe into particular model processes. Anomalies detected at the lowest levels can be traced to deficiencies in the model surface emission inventory, at mid-tropospheric levels to convective transport and horizontal advective diffusion, and at the upper tropospheric levels to model lightning NO$_x$ production and the placement of deeply transported NO$_2$ plumes such as from the Asian summer monsoon. The vertical information contained in the OMI cloud-sliced NO$_2$ profiles provides a global observational constraint that can be used to evaluate chemistry transport models (CTMs) and guide the development of key parameterization schemes.

1 Introduction

Global maps of tropospheric NO$_2$ vertical column densities (VCDs) derived from satellite UV–vis nadir sounders such as OMI, GOME and SCIAMACHY have contributed to the development of a variety of applications. Clear-sky observations of tropospheric NO$_2$ VCDs, those with cloud fractions typically below 25 %, have been used to constrain surface NO$_x$ emission inventories (Martin et al., 2003; Mijling and van der A, 2012; Miyazaki et al., 2012), detect and monitor

point source emission trends (Richter et al., 2005; van der A et al., 2008) and constrain surface NO$_2$ lifetimes (Beirle et al., 2011), to cite a few examples. Still, cloudy conditions predominate, which prevent the detection of NO$_2$ concentrations at the surface. For OMI, more than 70 % of the measurements collected in the extratropics are affected by clouds and typically discarded, with the consequent loss of information. The utilization of cloudy data from satellite IR and UV–vis nadir sounders provides access to a large repository of observations with potential to reveal information about trace gas concentrations at different altitudes and to constrain the parameterizations of a number of cloud-related processes.

Clouds are introduced in general circulation models (GCMs) because of their broadband radiative effects and direct relation with the water vapor feedbacks and precipitation (Jakob, 2003). Clouds also affect the redistribution of trace gases via convection and interaction with chemistry, which are essential elements in chemistry transport models (CTMs). Convective transport of polluted plumes (including NO$_x$, but also HO$_x$, CO and non-methane hydrocarbons – NMHCs) from the boundary layer can cause substantial enhancement of upper tropospheric ozone, an important anthropogenic greenhouse gas (Pickering et al., 1992). At high altitudes, enhanced chemical lifetimes and stronger winds are also responsible for the long-range transport of pollutants. Still, the exchange between environment and cloud air that determines the way that convective columns evolve (i.e., the entrainment and detrainment rates in mass flux schemes) remains uncertain. The presence of convective clouds not only transports pollutants vertically but also removes soluble species (like HNO$_3$) by precipitation, and modulates photolysis rates by altering the actinic fluxes above and below the

cloud (Tie et al., 2003). Associated with the deepest convective clouds, the production of NO$_x$ by lightning is a key component of the NO$_2$ budget in the upper troposphere, not only because of its relation with O$_3$ production but also because it affects the general oxidizing capacity of the atmosphere and the lifetimes of tracers destroyed by reactions with OH – like CO, SO$_2$ and CH$_4$. Yet the source strength and spatial distribution of lightning NO$_x$ emissions remain uncertain – with a global best estimate of $5 \pm 3 \, \text{Tg a}^{-1}$ (Schumann and Huntrieser, 2007).

In large-scale global CTMs, convection and other cloud-related processes such as scavenging and lightning NO$_x$ production are represented by subgrid parameterizations. Most convective parameterizations are tested against temperature and humidity profiles from radiosondes (Folkins et al., 2006), but chemical tracers provide additional constraints. A number of studies have tried to quantify the effect of different convective schemes on tropospheric CO and O$_3$ profiles using satellite-based climatologies for comparison with model data (Mahowald et al., 1995; Barret et al., 2010; Hoyle et al., 2011), finding the largest discrepancies in the tropical middle and upper troposphere. Even though NO$_2$ may appear unsuitable as a tracer of air motion because of its high reactivity with other NO$_y$ members (such as N$_2$O$_5$, HNO$_3$, PAN, NO$_3^-$ and HNO$_4$) and the presence of time-varying sources (mainly surface emissions and lightning NO$_x$, but also aircraft and stratospheric inflows), its short lifetime makes it attractive to study very fast transport mechanisms like convection. A number of studies have demonstrated the capabilities of satellite UV–vis sounders to estimate the source strength and 3-D distribution of lightning NO$_x$ over cloudy scenes (Boersma et al., 2005; Beirle et al., 2006; Martin et al., 2007; Miyazaki et al., 2014). These studies have found good agreement between modeled and observed lightning NO$_2$ over the tropical continents – albeit with discrepancies in the geographical and vertical distributions. Other studies have compared the performance of lightning parameterizations against satellite lightning flash densities, like Tost et al. (2007) and Murray et al. (2012), concluding that it is difficult to find a good combination of convective and lightning scheme that accurately reproduces the observed lightning distributions – leaving the problem of the NO$_x$ yield per flash aside. Thus there is a clear need for measurements with which the development of model parameterizations of convective transport and lightning NO$_x$ schemes can be guided.

In this paper, we use a variation of the cloud-slicing technique first developed by Ziemke et al. (2001) for tropospheric ozone, and later exploited by Liu et al. (2014) for tropospheric CO and Choi et al. (2014) for tropospheric NO$_2$, based on the increments of gas vertical column density above cloud as a function of cloud pressure within a certain longitude/latitude/time cell. Obviously, large cloud fractions and some degree of cloud height diversity within the cell are conditions required for this technique to produce useful results. The cloud-slicing approach applied by Choi et al. (2014) on

OMI NO$_2$ data was able to find signatures of uplifted anthropogenic and lightning NO$_2$ in their global free-tropospheric NO$_2$ concentrations, as well as in a number of tropospheric NO$_2$ profiles over selected regions. In this work, global annual and seasonal NO$_2$ volume mixing ratio (VMR) profiles are generated at a spatial resolution of $2° \times 2°$ on pressure levels centered at about 280, 380, 500, 620, 720 and 820 hPa. We give particular consideration to the scattering sensitivity of the OMI measurements above the cloud, as well as to the representativity of the cloud-sliced profiles with regard to a cloudy atmosphere. We report on results from this methodology as well as its direct applicability as an observational constraint using a state-of-the-art chemical transport model.

2 Methodology

The methodology to produce observed and modeled climatologies of tropospheric NO$_2$ VMR profiles under cloudy scenes begins with a description of the OMI and TM4 data sets involved. We introduce the pre-processing steps required to estimate NO$_2$ VCDs above cloud from OMI slant column measurements, followed by the upscaling steps required to bring the spatial resolution of the satellite observations in line with the TM4 model grid for comparison.

OMI NO$_2$ products

The NO$_2$ slant columns used in this work are retrieved by the UV–vis spectrometer OMI (Ozone Monitoring Instrument; Levelt et al., 2006) according to KNMI DOMINO version 2.0 (Boersma et al., 2007, 2011). The data files, which include total and stratospheric slant columns, averaging kernel information, cloud fraction, cloud pressure and assimilated trace gas profiles from the TM4 model, are available at http://www.temis.nl/airpollution/no2.html.

Of particular importance to this study are the cloud pressures and fractions retrieved by the OMI O$_2$–O$_2$ cloud algorithm (Acarreta et al., 2004). The OMI O$_2$–O$_2$ cloud algorithm uses an optically thick Lambertian cloud model with a fixed albedo of 0.8; the fraction of this Lambertian cloud model covering the pixel is called effective cloud fraction ($c_{\text{eff}} = (R_{\text{obs}} - R_{\text{clear}})/(R_{\text{cloudy}} - R_{\text{clear}})$, where R_{cloudy} and R_{clear} are modeled clear- and cloudy-sky reflectances, and R_{obs} is the observed continuum reflectance – i.e., the reflectance with the O$_2$–O$_2$ absorption line removed), which is not the same as the geometric cloud fraction but an equivalent amount that yields the same top-of-atmosphere (TOA) reflectance as observations; the altitude level of the Lambertian cloud model is then adjusted so that it results in the same amount of O$_2$–O$_2$ absorption as in observations (Stammes et al., 2008). The OMI O$_2$–O$_2$ cloud pressure refers to the optical radiative cloud pressure near the mid-level of the cloud and below the MODIS infrared-based cloud top, which is about 250 hPa higher than OMI for deep convective
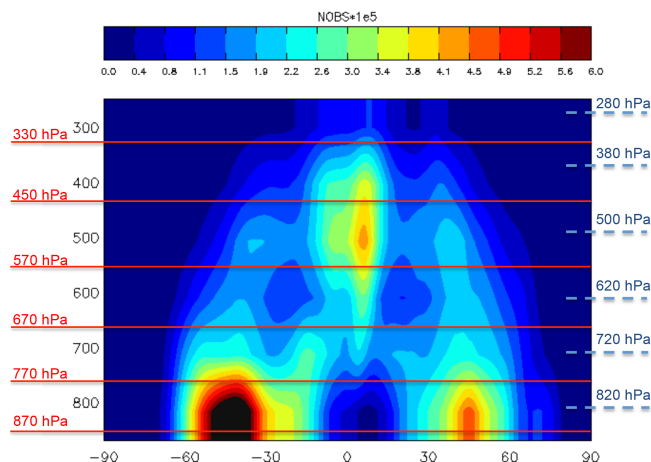
Table 1. Cloud pressure intervals and mean cloud pressure levels used for cloud slicing (hPa): the VCD pressure interval gives the boundaries of the cloud pressure bin. The VMR pressure interval refers to where the VMR is assumed constant after the pressure difference.

	VCD pressure interval	< VCD pressure >	VMR pressure interval	< VMR pressure >
Level 1	Tropopause–380	330	Tropopause–330	280
Level 2	380–500	450	330–450	380
Level 3	500–620	570	450–570	500
Level 4	620–720	670	570–670	620
Level 5	720–820	770	670–770	720
Level 6	820–1000	870	770–870	820

clouds or about 50–70 hPa higher for extratropical mid-level clouds. The OMI O$_2$–O$_2$ cloud pressure has been validated against PARASOL with a mean difference below 50 hPa and a SD below 100 hPa (Stammes et al., 2008). The OMI O$_2$–O$_2$ cloud fraction has been validated against MODIS with a mean difference of 0.01 and SD of 0.12 over cloudy scenes (effective cloud fractions larger than 50 % without surface snow or ice) (Sneep et al., 2008). In this paper, we use the cloud radiance fraction defined as CRF $= c_{\text{eff}} R_{\text{cloudy}} / R_{\text{obs}}$ – which represents the weight of the air mass factor of the cloudy part.

TM4 model

The TM4 chemistry transport model has a spatial resolution of 2° × 3° with 35 sigma pressure levels up to 0.38 hPa (and approximately 15 levels in the troposphere) driven by temperature and winds from ECMWF reanalyses and assimilated OMI stratospheric NO$_2$ information from previous orbits. The tropospheric chemistry scheme is based on Houweling et al. (1998) using the POET emissions (Olivier et al., 2003) database based on the EDGAR inventory for anthropogenic sources, which are typical of years 1990–1995, with biomass emissions of NO$_x$ based on ATSR fire counts over 1997–2003 and released in the lowest model layers. The photolysis rates are calculated as in Landgraf and Crutzen (1998) and modified as in Krol and van Weele (1997). In the TM4 model, the physical parameterization for convective tracer transport is calculated with a mass flux scheme that accounts for shallow, mid-level and deep convection (Tiedtke, 1989). Large-scale advection of tracers is performed by using the slopes scheme of Russell and Lerner (1981). The lightning NO$_x$ production is parameterized according to Meijer et al. (2001) using a linear relationship between lightning intensity and convective precipitation, with marine lightning 10 times less active than continental lightning and scaled to a total annual of 5 Tg N yr^{-1} (Boersma et al., 2005). The vertical lightning NO$_x$ profile for injection into the model is an approximation of the outflow profile suggested by Pickering et al. (1998). Including free-tropospheric emissions from air traffic and lightning, the total NO$_x$ emissions for 1997 amount to 46 Tg N yr^{-1}. More about this model may be found in Boersma et al. (2011) and references therein.

Figure 1. Latitude–height section of annual zonal mean OMI cloud frequencies (CRF > 50 %) – observed during daytime around 13:45 LST. On the left in red, the bottom pressure boundaries for the calculation of annual mean NO$_2$ VCDs above cloud (after Table 1). On the right in blue, the approximate pressure for the resulting NO$_2$ VMR after differentiation of VCDs (also after Table 1).

2.1 Cloud slicing

A technique initially developed for estimating upper tropospheric ozone using nadir sounders (Ziemke et al., 2001), cloud slicing consists in arranging collections of trace gas VCDs measured above clouds against cloud pressure over a certain area and time period in order to estimate a gas VMR via the pressure derivative as

$$\text{VMR} = 0.1 g \, \frac{M_{\text{air}}}{N_{\text{A}}} \cdot \frac{\partial \, \text{VCD}}{\partial p}, \qquad (1)$$

where $g = 9.8 \, \text{m s}^{-2}$, $M_{\text{air}} = 28.97 \, \text{g mol}^{-1}$ and $N_{\text{A}} = 6.022 \times 10^{23} \, \text{molec mol}^{-1}$ with VCD expressed in molec cm^{-2} and cloud pressure expressed in hPa. The method determines an average trace gas volume mixing ratio over a certain area, time period and cloud pressure interval (Choi et al., 2014). In this paper, annual average tropospheric NO$_2$ VCD lat–long grids from OMI and TM4 are produced for six tropospheric layers with bottom cloud pressures located within pressure intervals centered at about

330, 450, 570, 670, 770 and 870 hPa. The cloud pressure intervals used for cloud slicing were chosen after several trial runs and are laid out in Table 1 and Fig. 1. An annual climatology of NO$_2$ VMR profiles is then estimated after differencing the annual tropospheric VCD arrays above cloud with respect to pressure.

Figure 1 shows the latitude–height section of annual zonal mean OMI cloud frequency for the year 2006, showing that cloud slicing does not provide uniform global sampling. Most high clouds (mainly deep cumulus, since cirrus clouds pass generally undetected by OMI) occur along the Intertropical Convergence Zone (ITCZ) near the Equator and over tropical continents, but can also be seen in the mid-latitude storm track regions and over mid-latitude continents in the summer; mid-level clouds are prominent in the mid-latitude storm tracks, usually guided by the tropospheric westerly jets, and some occur in the ITCZ; and low clouds, including shallow cumulus and stratiform clouds, occur essentially over the oceans but are most prevalent over cooler subtropical oceans and in polar regions (Boucher et al., 2013). In summary, cloud sampling proves best at low to mid-altitudes in the extratropics and mid- to high altitudes in the deep tropics. However, cloud sampling is typically poor off the west coasts of subtropical (Pacific, Atlantic and Indian) landmasses at high altitudes – which are areas of large-scale subsidence with persistent low stratocumulus, and at low altitudes over the tropical landmasses, particularly the Amazon Basin and central Africa.

2.1.1   NO$_2$ above cloud

The tropospheric NO$_2$ vertical column density above the cloud, VCD$_{above}$, for an instrument like OMI is defined here as a function of the total slant column, SCD, as

$$VCD_{above} = \frac{(SCD - SCD_{strat} - SCD_{below})}{AMF_{above}}, \quad (2)$$

where SCD$_{strat}$ is the stratospheric slant column, SCD$_{below}$ accounts for the slant surface component leaked from below the cloud (i.e., the amount of surface signal that seeps through the cloud for partially cloudy conditions), and AMF$_{above}$ denotes the scattering sensitivity above the cloud. The stratospheric slant column arises from TM4 model stratospheric profiles assimilated to OMI observations over unpolluted areas (Belmonte Rivas et al., 2014). The below-cloud leaked component is defined as

$$SCD_{below} = (1 - CRF) \sum_{ground}^{CLP} m_{clear}(p) \cdot n(p) \cdot T_{corr}(p), \quad (3)$$

where CRF is the cloud radiance fraction, m_{clear} is the clear-sky component of the scattering sensitivity (purely dependent on Rayleigh scattering and surface albedo), $n(p)$ is the a priori trace gas profile (i.e., the TM4 model), and T_{corr} is the OMI temperature correction defined below. Note that the
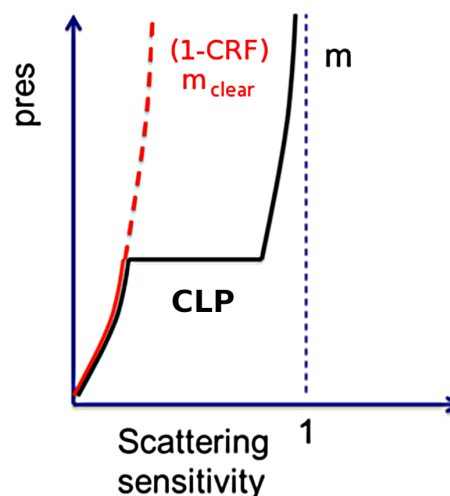

Figure 2. Schematic diagram of the scattering sensitivity above and below the cloud (normalized by the geometric air mass factor): CLP is the cloud level pressure, and m is the total scattering sensitivity, usually defined as $(1 - CRF)\, m_{clear} + CRF\, m_{cloudy}$. The red curve illustrates a residual sensitivity to NO$_2$ contents below the cloud when conditions are partially cloudy.

summation goes from the ground to the cloud level pressure, CLP (see Fig. 2), where the cloud level is given by the OMI O$_2$–O$_2$ cloud pressure.

The scattering sensitivity above the cloud, AMF$_{above}$, is defined as (see Appendix)

$$AMF_{above} = \frac{\sum\limits_{CLP}^{tropopause} m(p) \cdot n(p) \cdot T_{corr}(p)}{\sum\limits_{CLP}^{tropopause} n(p)}, \quad (4)$$

where m is the total scattering sensitivity (usually defined as $(1 - CRF)\, m_{clear} + CRF\, m_{cloudy}$ as in Boersma et al., 2004). Note that the summation in this case goes from cloud level to the tropopause (see Fig. 2). The total scattering sensitivity m has been derived from the averaging kernel AK(p) as

$$m(p) = \frac{AK(p) \cdot AMF}{T_{corr}(p)}, \quad (5)$$

where AMF is the total air mass factor (used to compute the total vertical column VCD $=$ SCD $/$ AMF from the total slant column SCD, and different from the tropospheric air mass factor AMF$_{trop}$ used to compute VCD$_{trop} =$ SCD$_{trop}$/AMF$_{trop}$). The temperature correction is defined as in Boersma et al. (2004) and accounts for the temperature dependence of the NO$_2$ absorption cross section and its influence on the retrieved slant column using ECMWF temperatures:

$$T_{corr}(p) = \frac{(220 - 11.4)}{[T(p) - 11.4]}. \quad (6)$$

The elements of the averaging kernel contain the height dependent sensitivity of the satellite observation to changes in tracer concentrations and they are calculated with a version of the Doubling Adding KNMI (DAK) radiative transfer model in combination with TM4-simulated tropospheric NO$_2$ profiles. Of central importance to our cloud-slicing approach is that a below-cloud leaked component (SCD$_{below}$) is removed from the tropospheric slant column, and a scattering sensitivity above the cloud (AMF$_{above}$) is used to estimate the vertical column density above the cloud, VCD$_{above}$. This is in contrast with the methodology applied in Choi et al. (2014), where below-cloud leakages are neglected (making tropospheric estimates more sensitive to surface contamination, particularly at low cloud fractions), and the scattering sensitivity above the cloud is assumed equal to the geometric air mass factor.

As far as model quantities are concerned, the NO$_2$ column above the cloud in TM4 is simply calculated as

$$\text{VCD}_{\text{above}} = \sum_{\text{CLP}}^{\text{tropopause}} n(p), \tag{7}$$

where $n(p)$ is the a priori trace gas profile (i.e., the TM4 model). Note that the a priori gas profiles, originally reported on hybrid sigma pressure grids, have been resampled onto a uniform pressure grid with steps of 23.75 hPa to simplify averaging operations. The cloud level pressure (CLP) that defines the model above-cloud NO$_2$ columns in Eq. (7) is the same OMI O$_2$–O$_2$ cloud pressure used for cloud slicing. Using OMI's cloud information to sample the TM4 model amounts to assuming that cloud altitudes and fractions in the model are identical to those observed by OMI. We know that differences between instantaneous model and observed cloud fields can be notable, but we also know that current model cloud fields are able to reproduce the average geographical and vertical distribution of observed cloud amounts reasonably well (Boersma et al., 2015), albeit with reports of underestimation of the low-level cloud fractions in the marine stratocumulus regions, underestimation of the mid-level cloud fractions everywhere, and slight overestimation of the high-level cloud fraction over the deep tropics (Nam et al., 2014) – errors that are likely related to the microphysical cloud and convection parameterizations. Therefore, using an observed cloud field to probe into model cloud processes, though probably suboptimal in case-by-case studies, is likely to be fine in an average sense.

2.1.2 Spatial averaging

A comparison of OMI observations with a model such as TM4 should also take into account the inhomogeneity of the tropospheric NO$_2$ field, which is usually large due to the presence of strong point sources and weather-scale variability. The model NO$_2$ columns should be viewed as areal averages, given that the limit of scales represented in the model is given by its resolution. Thus it is important to aggregate OMI observations to attain the same spatial resolution used by the model. The OMI NO$_2$ VCD above-cloud observations (with a nominal spatial resolution of 13 km × 24 km at the swath center) are aggregated onto daily 1° × 1° longitude–latitude bins – later spatially smoothed to 2° × 2° – before comparison with the afternoon TM4 model outputs defined on a 2° × 3° grid on a daily basis as in Eq. (7). The aggregated OMI product collects all VCDs observed within a specified period (1 day) with solar zenith angle less than 70°, surface albedo less than 30 % and CRF larger than 20 % at the OMI pixel level (roughly equivalent to an effective cloud fraction of 10 %, which is a minimum condition for cloud fraction and pressure to be properly reported by OMI). No weighting is applied. At this point, populating the grid bins with as many OMI measurements as possible is important in order to avoid spatial representation errors between the two records (a partially filled bin may not be representative of what occurs over the entire cell, which is what the model represents). The aggregated CRFs (and all other OMI and model quantities) are then evaluated at grid resolution, and a CRF threshold of 50 % at cell level is applied to both observations and model data. The annual mean tropospheric VCD above cloud is then calculated per pressure layer using the CLP thresholds specified in Table 1 on daily gridded OMI and TM4 NO$_2$ VCD outputs, provided there are at least 30 measurements in a bin.

2.1.3 Error analysis

In the cloud-slicing method, the derivation of annual mean VMR profiles from annual layered VCD amounts above cloud follows as

$$\langle \text{VMR}_i \rangle = \frac{C\left(\langle \text{VCD}_{i+1} \rangle - \langle \text{VCD}_i \rangle\right)}{\left(\langle p_{i+1} \rangle - \langle p_i \rangle\right)}, \tag{8}$$

where C is defined as $0.1 g M_{\text{air}}/N_{\text{A}}$ as in Eq. (1) and the index i refers to the cloud level. We term these objects VMR pseudoprofiles because they are constructed on the conditional provision of cloud presence, and the presence of cloud modifies the underlying NO$_2$ profile: either directly via chemical or dynamical processes such as lightning NO$_x$ production, advection of (clean/polluted) air from below, suppression of biomass burning or decreased photolysis under the cloud, or more indirectly via selective sampling of seasonal features, such as entangling a wet season column of enhanced lightning at high altitude with a dry season column of enhanced biomass burning at low altitude. One can appreciate that the effect of cloud presence on the profile varies with cloud altitude, which is unfortunate, because we use changes in cloud altitude to sample the underlying profile. This state of affairs introduces a source of systematic error between the cloud-slicing estimate (i.e., the pseudoprofile) and the actual underlying profile, which we term pseudoprofile error. One may evaluate (and further compensate for) the pseudo-

profile error associated with conditional cloud sampling by comparing the model VMR profile sampled using the cloud-slicing technique against the underlying "true" mean NO_2 VMR profile from the same model, as described below. Other sources of systematic error may also intervene, including uncertainties in the a priori corrections and errors in the stratospheric column. The effect of uncertainties in the a priori corrections is limited by the impact that a priori corrections have on pseudoprofiles, which is itself limited (see Supplement). The effect of errors in the stratospheric column is expected to be small, since stratospheric columns only show a small additive bias (Belmonte Rivas et al., 2014) that is bound to cancel via the pressure difference. One could also include temporal representativity errors from mismatched collocations between model and OMI clouds in this category, which Boersma et al. (2015) estimate to lie around 10 %. In this section we provide a brief description of the retrieval error that may be expected from instrumental random noise properties alone, followed by an estimate of pseudoprofile error that is based on model behavior.

Retrieval error

The retrieval error in the annual mean cloud-slicing profiles is assumed random and calculated by standard error propagation of Eq. (1). Note that we do not compute VMRs on daily or orbital basis (since one does not achieve the necessary cloud height diversity but in exceptional circumstances), but from the difference of annual mean VCDs. The derivation follows as

$$\delta\mathrm{VMR} = 0.1g\frac{M_{air}}{N_A}\delta\left(\frac{\partial\mathrm{VCD}_{annual}}{\partial p_{annual}}\right)$$
$$= 0.1g\frac{M_{air}}{N_A}\left(\frac{\delta\left(\mathrm{VCD}_1 - \mathrm{VCD}_2\right)}{p_1 - p_2}\right.$$
$$+ \frac{(\mathrm{VCD}_1 - \mathrm{VCD}_2)}{(p_1 - p_2)^2}\delta\left(p_1 - p_2\right)\right)$$
$$= 0.1g\frac{M_{air}}{N_A}\left(2\frac{\delta\mathrm{VCD}_{annual}}{p_1 - p_2}\right.$$
$$+ \frac{(\mathrm{VCD}_1 - \mathrm{VCD}_2)}{(p_1 - p_2)^2}2\delta p_{annual}\right),$$

where VCD_1, VCD_2, p_1 and p_2 are all mean annual quantities estimated for contiguous pressure levels. Assuming random Gaussian errors in the determination of single OMI observations with an uncertainty ($\delta\mathrm{VCD}$) of 50 % in the OMI vertical column density (Boersma, 2004) and an uncertainty (δp) of 100 hPa in O_2–O_2 cloud pressure (Stammes et al., 2008), the standard error of the mean annual quantity (VCD or pressure) is the standard error of the single retrieval divided by the square root of the number of OMI measurements collected per grid cell N_{grid} in a year:

$$\delta\mathrm{VCD}_{annual} = \delta\mathrm{VCD}/\sqrt{N_{grid}}$$
$$\delta p_{annual} = \delta p/\sqrt{N_{grid}}.$$

Thus we obtain

$$\delta\mathrm{VMR} = \tag{9}$$
$$0.1g\frac{M_{air}}{N_A}\left(2\frac{\delta\mathrm{VCD}}{\Delta p} + 2\frac{\Delta\mathrm{VCD}}{\Delta p}\cdot\frac{\delta p}{\Delta p}\right)\cdot\frac{1}{\sqrt{N_{grid}}}.$$

Pseudoprofile (systematic) error

The extent to which cloud-slicing profiles remain physical and accurate representations of an average cloudy atmosphere is limited by the assumptions that underlie the cloud-slicing difference, which can be expressed as

$$\mathrm{VMR}\,(p_{mid}) \propto \mathrm{VCD}(p < p_{dn}|p_{cloud} = p_{dn}) \tag{10}$$
$$- \mathrm{VCD}(p < p_{up}|p_{cloud} = p_{up}).$$

In cloud slicing, the mean VMR between the pressure levels p_{up} and p_{dn} is given by the difference between the VCD above cloud pressure p_{dn}, provided there is cloud at p_{dn}, and the VCD above cloud pressure p_{up}, provided there is cloud at p_{up} too. The problem is that the presence of cloud modifies the profile. One may think that the column difference in Eq. (10) is an approximation to what happens when clouds are located at p_{mid}, somewhere between p_{up} and p_{dn}. But assuming that the trace gas concentration profile does not change with small changes in cloud altitude (which are otherwise necessary to estimate the VMR slope) entails some error. Ideally, we would like to calculate

$$\mathrm{VMR}_{true}(p_{mid}) \propto \mathrm{VCD}(p < p_{dn}|p_{cloud} = p_{mid}) \tag{11}$$
$$- \mathrm{VCD}(p < p_{up}|p_{cloud} = p_{mid}).$$

Now we have a unique (and physically plausible) cloud condition behind the difference, $p_{cloud} = p_{mid}$, and a VMR estimate that is representative of gas concentration provided that there are clouds at the p_{mid} level. Yet if we would like to obtain a VMR estimate that is representative of trace gas concentration in a general cloudy atmosphere, then we would calculate

$$\mathrm{VMR}_{ref}(p_{mid}) \propto \mathrm{VCD}(p < p_{dn}|\forall p_{cloud}) \tag{12}$$
$$- \mathrm{VCD}(p < p_{up}|\forall p_{cloud}).$$

That is, VMR_{ref} represents a mean VMR profile provided that there are clouds anywhere in the column, i.e., regardless of cloud altitude. We refer to the difference between VMR and VMR_{true} as sampling error, because the cloud diversity necessary to estimate the trace gas concentration is distorting the underlying profile. We refer to the difference between VMR_{true} and VMR_{ref} as representation error, because a profile measured under high-cloud conditions is not representative of a profile under low-cloud conditions, nor in general representative of an average cloudy state. The sum of the sampling and representation errors, that is, the difference between the cloud-sliced VMR pseudoprofile and the
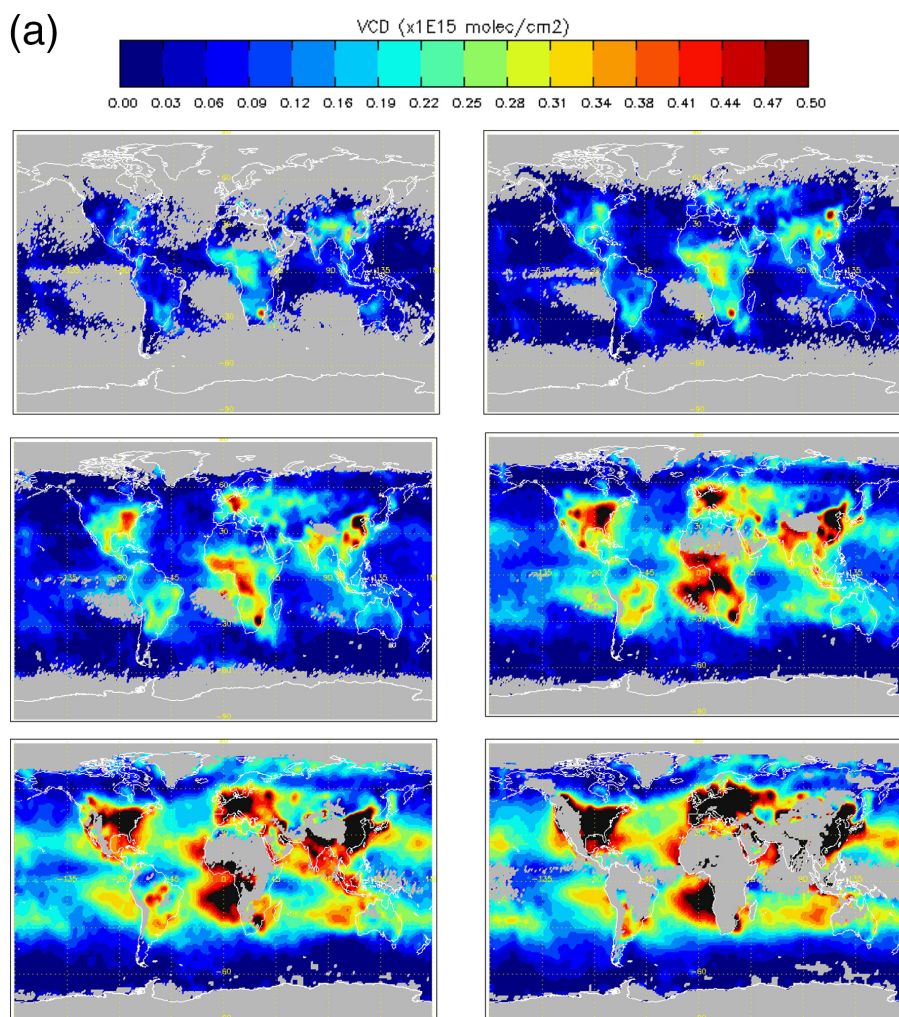
Figure 3.

average profile in a cloudy atmosphere VMR_{ref}, is what we call the pseudoprofile error. All VMR, VMR_{true} and VMR_{ref} profiles can be calculated on account of the TM4 CTM, so that a model-based estimation of the sampling and representation (pseudoprofile) systematic errors becomes available. The general pattern of pseudoprofile errors (see Sect. 3.3) indicates that biases are small in the upper three levels, largely positive (100–200 %) over tropical and extratropical outflows in the lower two levels, and negative (up to 100 %) over the continents for the lower three levels (particularly over central and South America, Australia, Canada and Siberia). One way to bypass this systematic error is to scale the observed VMR pseudoprofiles by the model profile-to-pseudoprofile ratio as

$$VMR_{ref,OMI} = VMR_{OMI} \left(\frac{VMR_{ref,TM4}}{VMR_{TM4}} \right). \tag{13}$$

This model-based pseudoprofile correction (applied in Sect. 3.4) remains subject to the accuracy with which the

model represents its own profiles, and should be treated with caution.

3 Results and discussion

3.1 NO₂ VCD above cloud

Figure 3a shows the annual mean tropospheric NO₂ VCD aggregates on $1° \times 1°$ grids observed by OMI for the year 2006 above clouds with mean pressures centered at around 330, 450, 570, 670, 770 and 870 hPa – see Fig. 1 and Table 1. A similar set of annual mean NO₂ VCDs above cloud has been extracted from the TM4 model using identical cloud sampling (i.e., using the cloud fraction and cloud pressure from OMI) for comparison (see Fig. 3b).

Most of the lightning NO₂ emissions are expected above clouds higher than 450 hPa (i.e., the upper two levels in Fig. 3a), although some deep convection may also be present over strong industrial sources (like the northeastern USA,
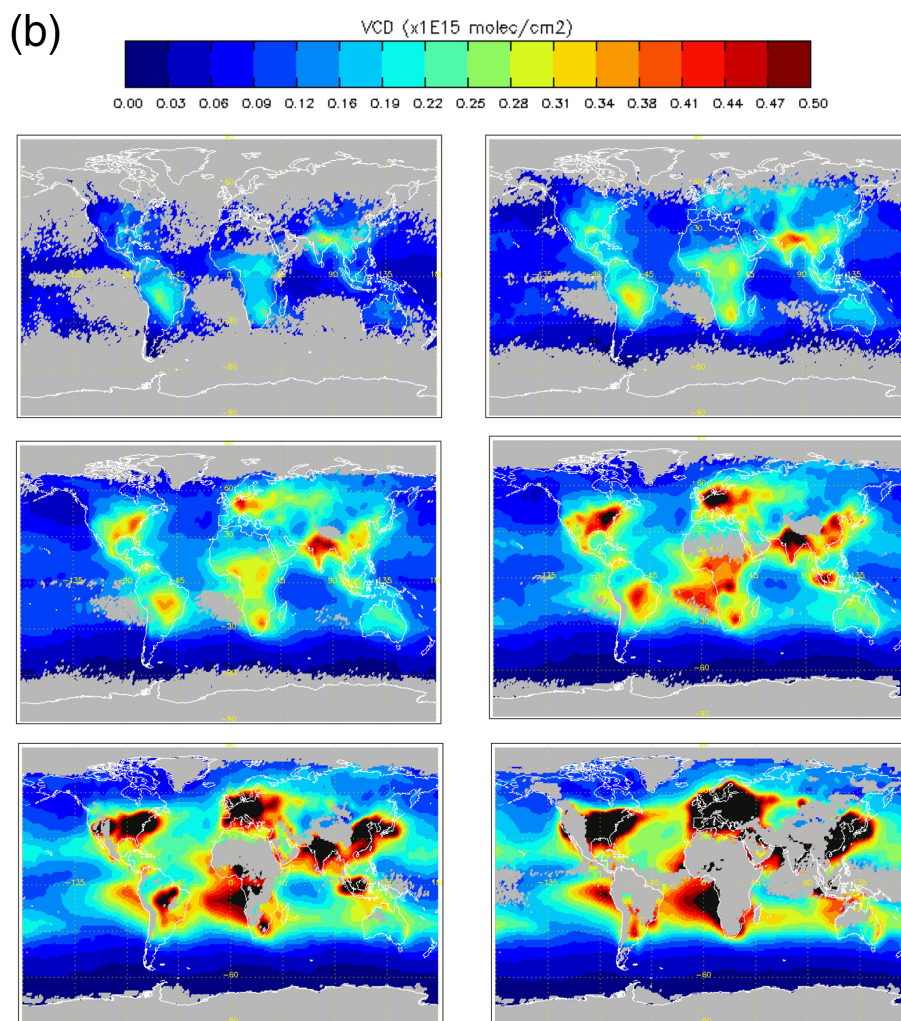
Figure 3. (a) OMI NO$_2$ VCDs above cloud – average quantities for the year 2006: for high-altitude clouds (top row, 330 and 450 hPa), mid-altitude clouds (middle row, 570 and 670 hPa) and low clouds (bottom row, 770 and 870 hPa). Gray means no data available (i.e., insufficient number of cloud detections in the cell). **(b)** Same as **(a)** but for TM4.

Europe, China, and the Johannesburg, South Africa, area) or biomass burning sources in central Africa, the Amazon Basin or northeastern India, complicating the problem of process attribution.

The two middle levels in Fig. 3a are expected to carry, along with the NO$_2$ burden inherited from the upper levels, additional signatures from frontal uplifting into the mid-troposphere by conveyor belts over major industrial sources in the northeastern USA, central Europe and China, as well as convective transport of biomass burning sources over central Africa, South America, Indonesia and northern Australia. The strong convective signatures of surface industrial and biomass burning sources, along with their low tropospheric outflows, dominate the two lowest levels in Fig. 3a. Note the extensive lack of data over the tropical continents at low altitudes, a region where persistent high cloud precludes pene-

tration into the lowest levels, and over the subtropical subsidence areas.

By differencing the annual average VCD arrays with respect to pressure, we expect to separate the contributions from different altitudes to the total tropospheric column. But before that, let us take a look at the scattering sensitivities above cloud and the effects of correcting for below-cloud leakage in these results. Figure 4 shows the annual mean tropospheric scattering sensitivity above cloud level (AMF$_{above}$ in Eq. 4) applied to generate the OMI NO$_2$ VCDs shown in Fig. 3a. Globally, the tropospheric scattering sensitivity above the cloud does not deviate by more than 10 % from the geometric air mass factor at most cloud altitudes, except at the lowest levels, where it suffers reductions of up to 30 %. This reduction in scattering sensitivity at the lowest cloud levels may come as a surprise, particularly when clouds are known to boost the scattering sensitivity just above the cloud
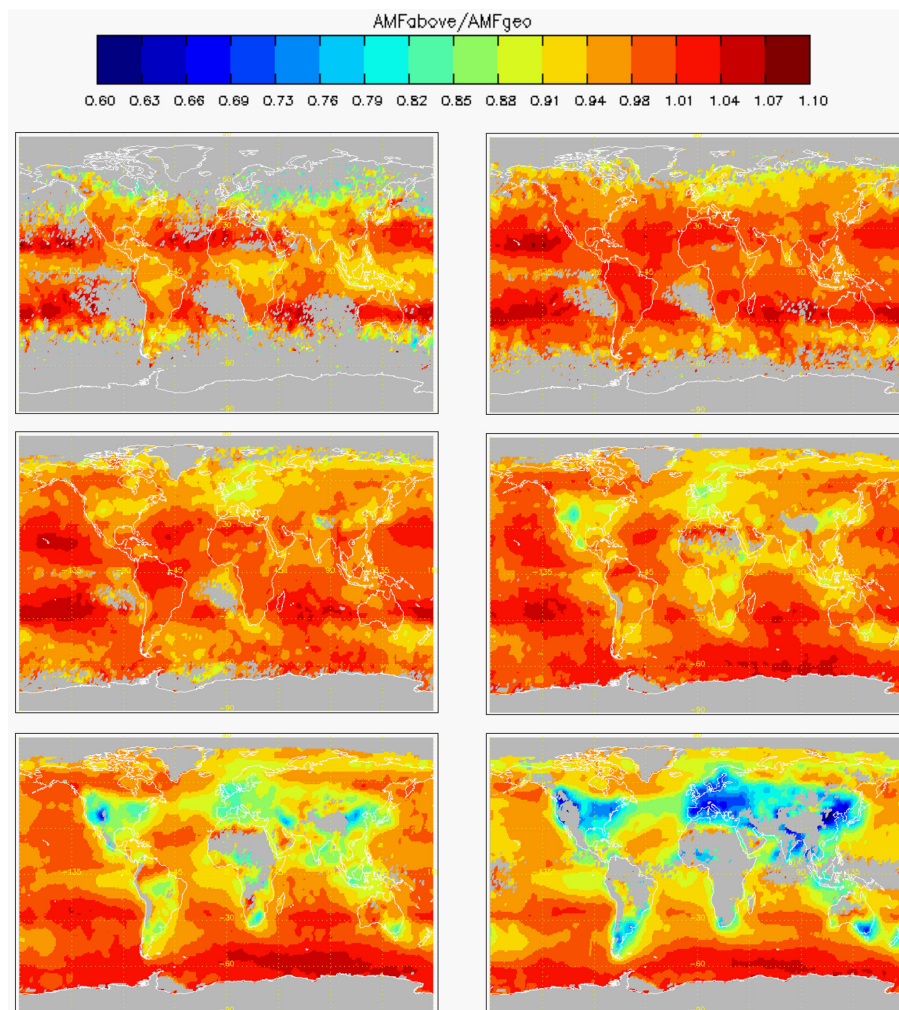
Figure 4. Tropospheric scattering sensitivities above cloud level (AMF$_{above}$/ AMF$_{geo}$ in Eq. 4): for high-altitude clouds (top row, 330 and 450 hPa), mid-altitude clouds (middle row, 570 and 670 hPa) and low clouds (bottom row, 770 and 870 hPa).

top. However, the pronounced decrease in scattering sensitivity at the lowest cloud levels is related to penetration of substantial amounts of NO$_2$ (from strong or elevated surface sources) into the cloud mid-level, where extinction acts to reduce the scattering sensitivity. Other than the extinction effect, the variability in scattering sensitivity is governed by changes in the observation geometry (AMF$_{above}$ decreases as the sun angle increases) and the temperature correction introduced in Eq. (6), which is responsible for the subtropical bands and the variability at high southern latitudes.

The corrections for the surface leaked component introduced in Eq. (3) are largest (see Supplement) over polluted regions for the highest clouds (up to 50–66 %) and smallest over clean areas like the oceans. In order to verify that the model-based below-cloud leak corrections do not appreciably change the OMI NO$_2$ VCDs arrays, we have performed a separate trial run where the CRF threshold (at grid level) is increased from 50 to 80 % (see Supplement) to conclude

that none of the prominent VCD signatures seen in Fig. 3a (or none of the VMR features that we will see later) changes appreciably in the restricted CRF > 80 % case. Results from the CRF > 80 % trial run include notably diminished cloud frequencies and spatial coverage, seriously thinning the population that produces the annual averages and generally damaging their representativity. This effect is particularly notable in the upper two levels (280 and 380 hPa) and to lesser extent over the large-scale subsidence area in the lowest level, since deep convective and low marine stratocumulus clouds are not particularly extensive but have a preference for low effective cloud fractions. Excluding the contributions from these cloud types in the CRF > 80 % case does not change the mid-tropospheric NO$_2$ patterns relative to the CRF > 50 % case, but it biases the OMI aggregates in the upper troposphere low relative to the modeled average, which is not particularly sensitive to this change. In summary, the CRF > 80 % trial run does not show any clear signs of a priori information
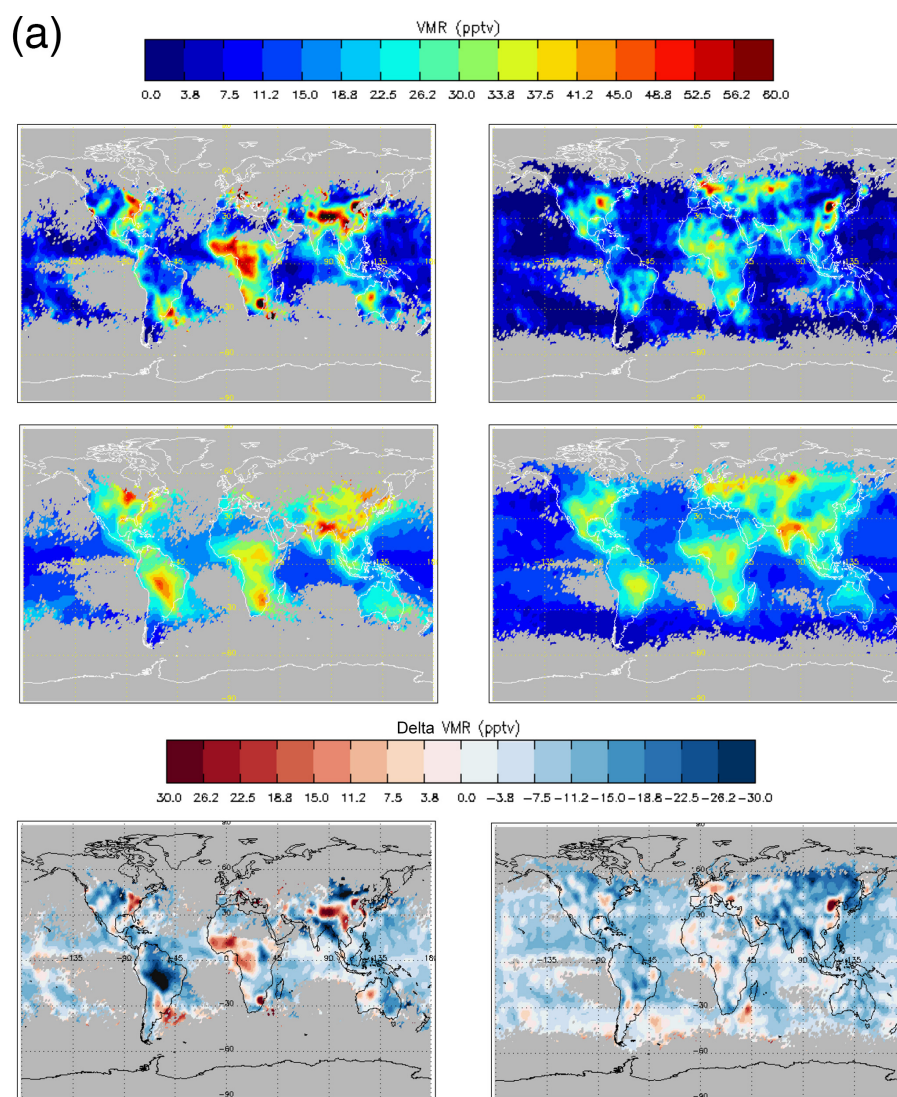
(a)

Figure 5.

constraining the results, but it provides hints of results being influenced detrimentally by the lower sampling densities afforded by a higher CRF threshold.

3.2 NO₂ VMR pseudoprofiles

The annual mean tropospheric NO_2 VMR pseudoprofiles observed by OMI for the year 2006 are compared against their TM4 model counterparts in Fig. 5a–c. Note that pseudoprofile errors do not affect this comparison, since both observed and modeled pseudoprofiles are observing identical (if somewhat unphysical, because of sampling and representation issues) atmospheric states. After the pressure difference, there remain some instances where negative VMRs are found, but these are mainly associated with poorly populated cells (such as at high latitudes, near the tropics at low altitudes, or around subsidence regions). These instances are identified and dealt

with by recourse to information from nearby cells, when available, or otherwise ignored.

Many of the cloud-slicing features observed at the upper two levels (280 and 380 hPa) in Fig. 5a can be attributed to actual biomass burning, lightning and deep convection. It may be difficult to separate these components clearly without a proper seasonal analysis (deferred to Sect. 3.6), although one can identify areas of predominant lightning production as those regions that do not seem connected via convection to surface sources underneath and use the LIS-OTD flash rate climatology and the ATSR fire counts (see Fig. 6 below) as interpretation aids for attribution. Positive anomalies (observations larger than modeled amounts) are detected in Fig. 5a over all major industrial areas (eastern USA, central Europe and eastern China) both at 280 and 380 hPa levels, suggesting that deep transport of boundary layer NO_2 may be too weak in the model. However, there are extensive neg-
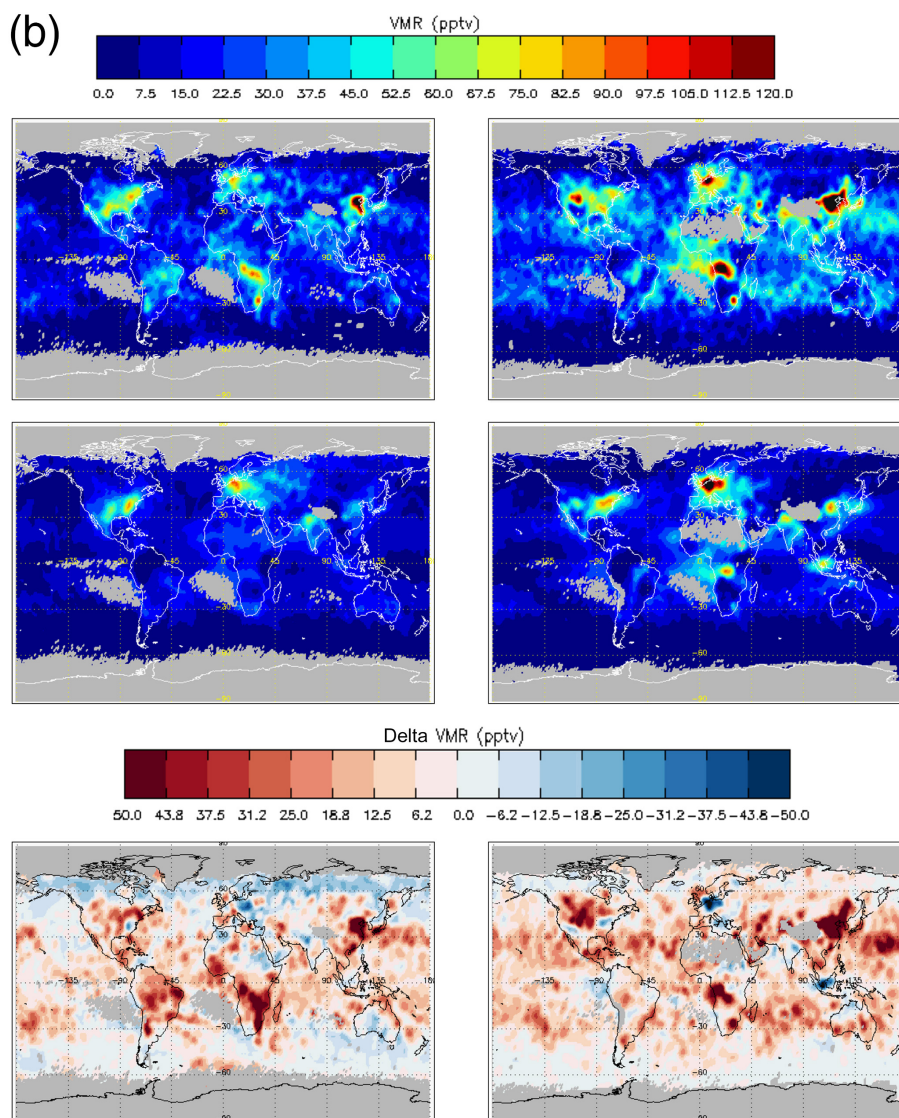
Figure 5.

ative anomalies (meaning observations lower than modeled amounts) in background upper tropospheric NO$_2$ both at 280 and 380 hPa, which is consistent with reports of model over-estimation of the amount of NO$_2$ attributed to lightning over the tropical oceans in Boersma (2005).

Negative anomalies in Fig. 5a are particularly large over Siberia, Amazonia and the Bay of Bengal. The negative anomaly over eastern Siberia, an area of predominant biomass burning, could be related to excessive fire-induced NO$_2$ emission over boreal forests in the model (Huijnen et al., 2012). In South America, lightning NO$_2$ contributions seen by OMI appear confined mostly to the western equatorial coast (Peru, Ecuador and Colombia) on the one hand, and southern Brazil and off the east coast of Uruguay on the other hand (more in line with the LIS-OTD flash climatology shown in Fig. 6) – in stark contrast with model amounts,

which locate the lightning maximum further to the north over the Brazilian Matto Grosso, where the maxima in precipitation related to the South American monsoon system usually takes place. It is worth noting that the lightning intensity in the TM4 model is solely driven by convective precipitation, although Albrecht et al. (2011) report that convective precipitation is not always well correlated with lightning in this area, showing that the most efficient storms in producing lightning per rainfall are located in the south regions of Brazil. The negative anomaly over Amazonia is therefore very likely related to problems with the TM4 lightning scheme. The negative anomaly over the Bay of Bengal, an area of maxima in precipitation related to the Indian monsoon, could also be a reflection of excess model lightning linked to convection.

Other notable discrepancies in Fig. 5a include positive anomalies over central Africa and northeastern India at
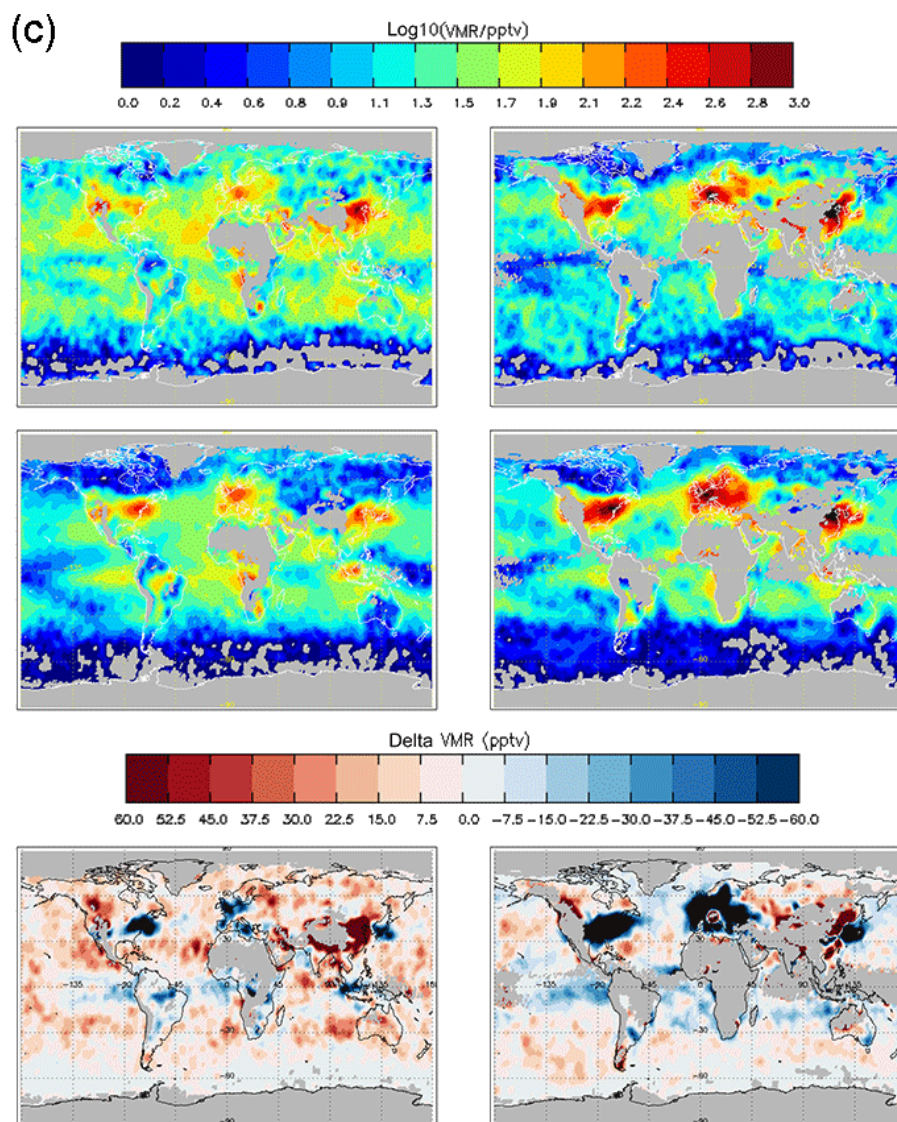
Figure 5. (a) Upper cloud levels (280 hPa left, 380 hPa right): OMI vs. model NO$_2$ VMRs (OMI top, TM4 middle, difference bottom) average quantities for the year 2006. **(b)** Same as **(a)** but for middle cloud levels (500 hPa left, 620 hPa right). **(c)** Same as **(a)** but for lower cloud levels (720 hPa left, 820 hPa right).

280 hPa. Over central Africa, the pattern of positive anomalies bears only partial resemblance to the pattern of biomass burning emission underneath (see mid-level OMI VMRs in Fig. 5b) – suggesting that upper level positive anomalies in central Africa may be related more to deficiencies in the lightning scheme than to convective transport. Actually, Barret et al. (2010) report that lightning flash frequencies simulated by TM4 are lower than measured by the LIS climatology over the southern Sahel, which is consistent with our observations. On the other hand, the large positive anomaly observed over the Tibetan Plateau at 280 hPa, which significantly deviates from the LIS-OTD flash rate climatology in the area (confined to the Himalayan foothills only), is very likely an effect of deep transport associated with the Asian

monsoon. The model does show an enhancement in upper tropospheric NO$_2$ over India, but not moving far enough north into the Tibetan Plateau and failing to reproduce the strong enhancements in upper tropospheric NO$_2$ over northeastern India and southern China related to the Asian summer monsoon plume – which Kar et al. (2004) also detected in the MOPITT CO profiles.

The cloud-slicing features observed at the midtropospheric levels (500 and 620 hPa) in Fig. 5b may be mostly attributed to mid-tropospheric convection of strong surface sources and their associated outflows. We observe a remarkable agreement between model and observations on the localization and intensity of major convective signals over industrial sources (eastern USA,
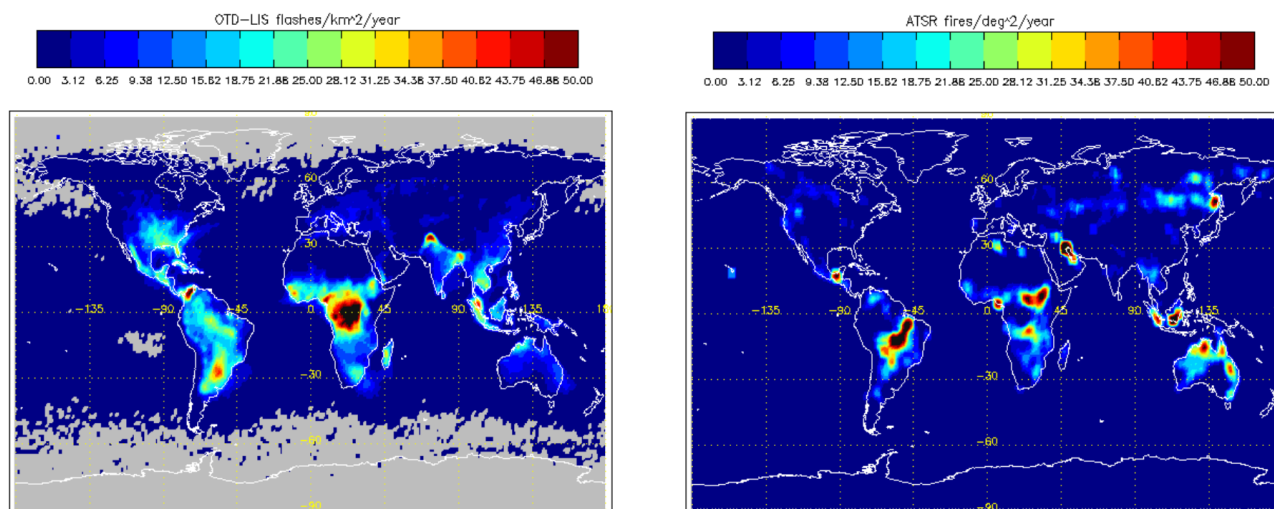
Figure 6. Interpretation aids for process attribution: mean flash rate climatology (1998–2010) from the LIS-OTD sensor (left; Cecil et al., 2014) and fire count climatology (1997–2003) from the ATSR sensor (right; Arino et al., 2012).

central Europe, China and India) as well as over typical biomass burning sources in central Africa, Indonesia and South America. Contrary to what is observed in the upper levels (see prevalent negative anomalies in Fig. 5a), there are extensive positive anomalies (meaning observations larger than modeled amounts) in background middle tropospheric NO$_2$ both at 500 and 620 hPa in Fig. 5b, particularly over the tropics and subtropics – which is indicative of deficient model mid-tropospheric outflows at these levels. Positive anomalies over the continents are particularly large over China (with an outflow-related positive anomaly downwind over the Pacific), the central USA, and the biomass burning regions in central Africa and South America. While it may be more or less clear that enhanced mid-tropospheric NO$_2$ concentrations observed over the oceans are related to enhanced convective inflows into this level (without definitely discarding a problem with NO$_2$ lifetime), the origin of the convective anomalies remains ambiguous. A cursory look at the NO$_2$ concentrations observed at lower levels might help determine whether flux anomalies into the mid-troposphere are related to deficiencies in model-prescribed surface emissions or problems with the convective transport scheme, or both.

For example, the pattern of anomalies over China at lowest levels (see Fig. 5c) is prominently positive, but it carries a dipolar positive–negative (China–Japan) pattern that is no longer observed at higher levels. Thus, while it is possible that some of the mid-tropospheric convective anomalies are a response to flux anomalies carried from underneath (i.e., a deficiency in the originally prescribed surface emission), as happens over the eastern USA and Europe, where negative anomalies are carried upwards (see Fig. 5b), the overall effect does not exclude net deficiencies in model convective transport. As far as biomass burning is concerned, the pat-

tern of anomalies over central Africa and South America in the lowest tropospheric levels (see Fig. 5c) is unfortunately not as evident (given the lack of low-cloud detections) as over China but mostly neutral or slightly negative, indicating that mid-tropospheric positive anomalies in this area respond to either a convective transport scheme that is too weak or a model injection height that is too low.

The lower tropospheric levels (720 and 820 hPa) in NO$_2$ sampled by the cloud-slicing technique are shown in Fig. 5c. These levels sustain the highest NO$_2$ concentrations in the vicinity of major industrial hubs (eastern USA, central Europe and China) and the strongest anomalies as well, which in this case can be linked directly to deficiencies in prescribed surface emissions. All major features in the anomaly patterns at these levels can be matched unambiguously to the pattern of OMI to TM4 total tropospheric NO$_2$ column differences for clear-sky conditions shown later in Fig. 12, characterized by positive anomalies over the northeastern USA, central Europe and Japan, and negative anomalies over China. These low-level signatures are consistent with NO$_2$ increases over China, India and the Middle East, and NO$_2$ decreases over the eastern USA and central Europe, which are not reflected in the model emission inventory. Other salient features at these levels include an interesting band of negative anomalies along the ITCZ (perhaps related to rapid convective mixing of relative "clean" air from the boundary layer) and extensive positive anomalies over the oceans (more so at 720 than at 820 hPa) – revealing deficient model outflows at high latitudes and suggesting that poleward transport of NO$_2$ in the model may not be vigorous enough (a problem likely related to horizontal diffusion in the model).

In summary, there is remarkable agreement between observed and modeled upper/middle/lower tropospheric NO$_2$ amounts, their main distributions resembling each other at
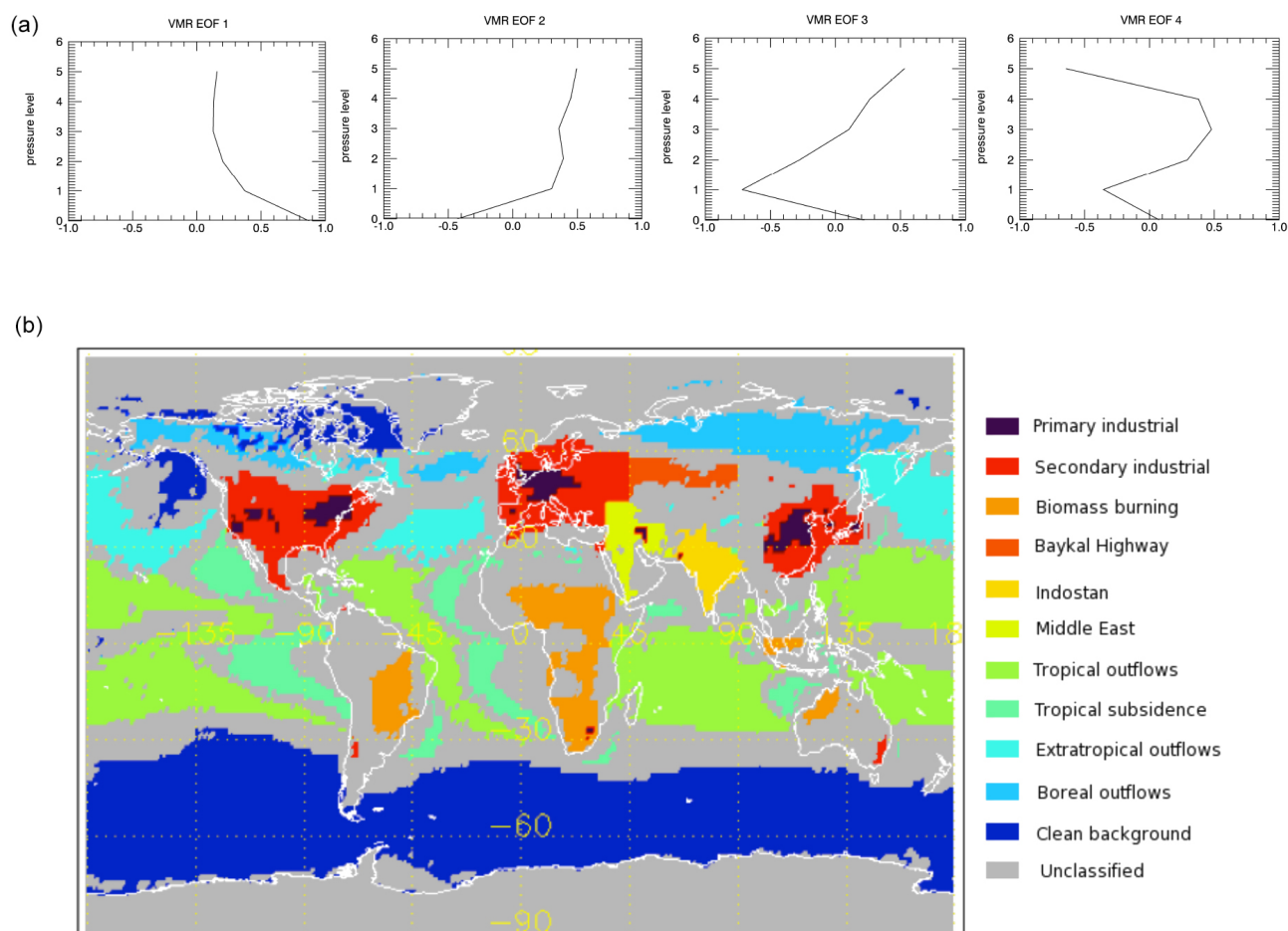
(a)

(b)

Figure 7. (a) Classification EOFs: surface source, outflow, high/low outflow, and middle outflow. **(b)** Model-based classes based on EOF decomposition of model NO$_2$ profiles under cloudy conditions: black (primary industrial), red (secondary industrial), orange (biomass burning), ochre (Baykal Highway), yellow (Indostan), light green (Middle East), green (tropical outflow), turquoise (tropical subsidence), cyan (extratropical outflow), blue (boreal outflow), and dark blue (clear background). Gray means unclassified.

continental scale, with localized differences suggesting that the cloud-slicing technique holds promise for testing model features related to anthropogenic emission, convection and uplift, horizontal advection and lightning NO$_x$ production.

3.3 Classification

In the previous section, we studied the geographical distribution of observed and modeled NO$_2$ amounts on different pressure layers. In this section, we focus on the vertical dimension by looking at NO$_2$ VMR amounts across pressure layers. In order to simplify the analysis, we have defined a set of geographical classes based on the amount of variance contained in the TM4 model NO$_2$ profiles. These classes characterize how much of the NO$_2$ content in the profile can be apportioned to surface sources and how much to outflows – further subdivided into outflows with low-, mid- or high-altitude components. Annual mean NO$_2$ VMR profiles are plotted for each class, along with reference to pseudoprofile error.

A standard empirical orthogonal function (EOF) decomposition of the reference TM4 profiles (VMR$_{ref}$ in Eq. 12) is employed to characterize the geographical variance of NO$_2$ vertical profiles under cloudy conditions and identify major spatial patterns. The first four EOF eigenvectors (out of a total of six) are shown in Fig. 7a. The first EOF represents profiles with higher concentrations near the surface – a profile over a surface source. The second EOF represents profiles with concentrations uniformly distributed across the column – a profile for a generic outflow type. The third and fourth EOF eigenvectors divide the generic outflow type into subtypes with stronger high-altitude (EOF3 > 0), low-altitude (EOF3 < 0) or mid-tropospheric (EOF4 > 0) components. The classes that result from applying masks based on the conditions defined in Table 2 are shown in Fig. 7b. According to the TM4 model, the classes containing all primary and secondary industrial sources (i.e., strong projections on EOF1) are mainly confined to the USA, Europe and China. Other secondary industrial sources relate to India, the Middle East

Table 2. Model-based source and outflow class definitions based on EOF decomposition.

Class label	Main condition	Extra condition
Primary industrial	EOF1 > 400 pptv	USA, Europe, China
Secondary industrial	100 pptv < EOF1 < 400 pptv	USA, Europe, China
Biomass burning	100 pptv < EOF1 < 400 pptv	geographic
Baykal highway	100 pptv < EOF1 < 400 pptv	geographic
Indostan	100 pptv < EOF1 < 400 pptv	geographic
Middle East	100 pptv < EOF1 < 400 pptv	geographic
Tropical outflow	EOF1 < 50 pptv, EOF2 > 15 pptv	EOF3 > 0, EOF4 > 0
Tropical subsidence	EOF1 < 50 pptv, EOF2 > 15 pptv	EOF3 < 0
Extratropical outflow	EOF1 < 50 pptv, EOF2 > 15 pptv	EOF3 > 0, EOF4 < 0
Boreal outflow	EOF1 < 50 pptv, EOF2 > 15 pptv	EOF3 ≫ 0
Clean background	EOF1 < 15 pptv, EOF2 < 15 pptv	

and the Baykal Highway (a major road connecting Moscow to Irkutsk, passing through Chelyabinsk, Omsk and Novosibirsk). Major biomass burning sources include large sectors in Africa and South America, Indonesia, New Guinea, and northern Australia. NO_2 outflows over the tropics (i.e., strong projections on EOF2) are subdivided into generic tropical outflows (with strong upper and mid-tropospheric components, or larger projections on EOF3 and EOF4) and outflows over large-scale subsidence areas (with stronger lower tropospheric components, or negative projections on EOF3). The extratropical outflows differ from the tropical outflows in that the sign of the mid-tropospheric projection is reversed, so that extratropical profiles are more C-shaped (according to the model). The boreal outflow differs from the extratropical outflow in that it has an extremely large upper tropospheric component (i.e., a very large projection on EOF3). Finally, we have defined a separate class, labeled clean background, including all those areas without significant projections on either source or outflow eigenvectors.

The average tropospheric NO_2 profiles estimated using the cloud-slicing method on OMI and TM4 data sets for all the 11 classes (15 classes when primary and secondary industrial regions are subdivided geographically into China, USA and Europe subclasses) defined in Table 2 and Fig. 7b are shown next in Figs. 8 and 9. These plots compare the OMI and TM4 VMR pseudoprofile estimates calculated in a cloud-slicing fashion as in Eq. (10), along with the reference TM4 VMR_{ref} profile calculated as in Eq. (12) for an average cloudy atmosphere. Recall that the difference between the TM4 VMR and VMR_{ref} profiles gives an indication of pseudoprofile error – or the representativity of the cloud-slicing estimate relative to a general cloudy situation. The OMI VMR cloud-slicing estimate is bounded by error bars calculated from standard error propagation as in Eq. (9), and scaling by the square root of the number of profiles collected per grid cell – also shown in right subpanels in Figs. 8 and 9.

The cloud-slicing estimates for the annual tropospheric NO_2 profiles over primary industrial centers in the eastern USA, Europe and China are shown in the first row in Fig. 8.

There is a remarkably good correspondence between observed and modeled tropospheric NO_2 profiles over these strongly emitting areas, particularly over central Europe, attesting to the accuracy and representativity of the cloud-slicing estimates for yearly means. Pseudoprofile errors are small in these areas, so that cloud-slicing estimates remain a good representation of average cloudy conditions. The OMI to TM4 VMR differences at the lowest levels are consistent with known deficiencies in model-prescribed surface emissions (OMI smaller than TM4 over the eastern USA and central Europe, but larger over China). These low-level anomalies are carried upwards to a level of 500–600 hPa, above which the effects of enhanced convective mid-tropospheric and deep transport start to dominate regardless of the signature of the surface difference. The second row in Fig. 8 shows the annual tropospheric NO_2 profiles over secondary industrial centers around eastern USA, Europe and China. The low-level features related to surface emission are identical to those of the primary centers, but the signature of enhanced mid-tropospheric convection is clearer – indicating that vertical transport in the model is too weak or lifetime too short, regardless of the sign of the surface anomaly. The sign of the OMI to TM4 difference is reversed in the upper two levels, in line with the generalized model overestimation of NO_2 in the upper troposphere. The third row in Fig. 8 shows the cloud-slicing estimate for the annual tropospheric NO_2 profiles over secondary industrial pollution centers in India, the Middle East and the Baykal Highway – note that pseudoprofile errors are larger in this case. For India, the differences between OMI and TM4 profiles at low levels point to a large underestimation of model surface emissions, and model overestimation of upper tropospheric NO_2 amounts – this upper level anomaly related to the misplaced Asian summer monsoon signal, which in observations appears located over the Tibetan Plateau. For the Middle East, the difference between OMI and TM4 profiles points to large differences at mid-tropospheric level (OMI larger than TM4). The agreement between OMI and TM4 profiles for the Baykal Highway class is reasonably good – allowing for a small un-
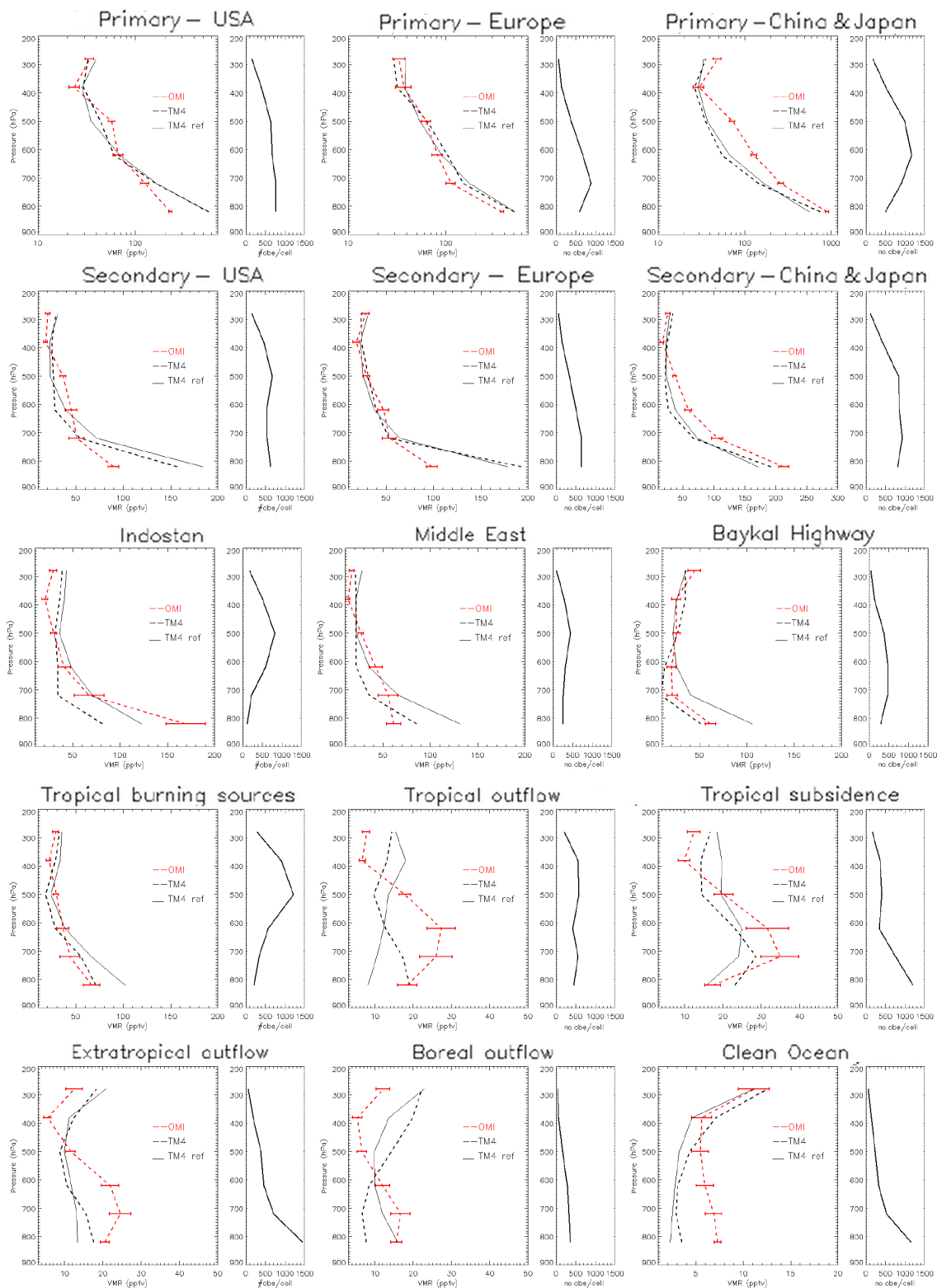
Figure 8. Cloud-slicing NO$_2$ VMR profiles for the year 2006 by class (OMI pseudoprofile, dashed red line; TM4 pseudoprofile, dashed black line; TM4 profile for cloudy conditions, continuous black line). The error bars show random retrieval errors. The differences between continuous and dashed black lines show systematic pseudoprofile errors. The subpanels on the right show the average number of OMI observations collected per grid cell per year for that class.
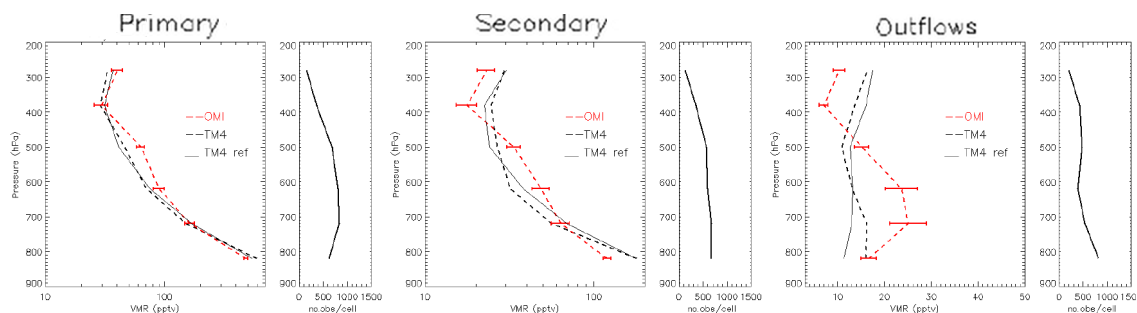
Figure 9. Cloud-slicing NO_2 VMR profiles for year 2006 by class: all primary sources (left), all secondary sources (middle) and all outflow classes (right). (OMI pseudoprofile, dashed red line; TM4 pseudoprofile, dashed black line; TM4 profile for cloudy conditions, continuous black line). The error bars show random retrieval errors. The differences between continuous and dashed black lines show systematic pseudoprofile errors.

derestimation of model surface emissions. After deep transport in China, this is the class with higher upper level NO_2 amounts, most likely related to fire-induced convection from boreal fires. The left panel in the fourth row in Fig. 8 shows the cloud-slicing estimate for the annual tropospheric NO_2 profile over tropical biomass burning regions, featuring positive anomalies at middle levels and negative anomalies at lower and upper levels, again pointing at defective model convective transport into the mid-troposphere (or issues with the pyro-convection height). The cloud-slicing estimates for annual tropospheric NO_2 profiles over typical outflow regions are shown in the middle and right panels in the fourth row (tropical and tropical subsidence outflows) and left and middle panels in the fifth row (extratropical and boreal outflows) in Fig. 8. As a salient feature, all of the outflow profiles share a prominent mid-tropospheric plume centered at around 620 hPa in the tropics and a little lower in the extratropics, around 720 hPa, with NO_2 amounts much smaller than the model in the upper troposphere and general agreement at the lowest level, producing profiles which are generally S-shaped (instead of C-shaped as in the model). The mid-tropospheric plume is likely related to enhanced convective fluxes of NO_2 over industrial and biomass burning areas (but definitely not discarding issues with NO_2 lifetime or substantial chemical NO_x recycling from HNO_3 and PAN sources at this level). Note also the generalized model overestimation of NO_2 in the upper levels (tropical and extratropical), which is consistent with reports of excess lightning NO_x production over the tropical oceans in Boersma et al. (2005). The upper level overestimation is particularly large for the boreal outflow class, which we also mentioned could be related to the excess fire-induced convection over Siberia or too large NO_x emission factors. Finally, the cloud-slicing estimate for the annual tropospheric NO_2 profile over the clean Southern Ocean is shown in the right panel of the last row in Fig. 8, with good agreement at the top levels and gradually increasing model underestimation towards the surface, sug-

gesting enhanced lateral contributions at high latitudes from horizontal eddy diffusion.

The left panel in Fig. 9 shows the annual tropospheric NO_2 profile for all the primary surface sources together (eastern USA, central Europe and China), indicating that differences at surface level average out globally, leaving the effects of enhanced observed mid-tropospheric convection and deep transport to stand out. The signature of enhanced mid-tropospheric convection becomes even clearer in the middle panel in Fig. 9, which shows the annual tropospheric NO_2 profile for all secondary surface sources together (around primary sources, plus India, the Middle East, the Baykal Highway and the biomass burning areas), where the signature of enhanced deep transport is in this case replaced by model overestimation of upper tropospheric NO_2. The model overestimation of upper level NO_2 appears clearly in the right panel in Fig. 9, which shows the annual tropospheric NO_2 profile for all the outflow classes, along with a prominent model underestimation of mid-tropospheric NO_2 levels. In summary, and consistent with our comments on Fig. 5a–c, the average profiles that result from applying the cloud-slicing technique on observed OMI and modeled TM4 data sets show striking overall similarities, which confer great confidence to the cloud-slicing approach, along with more localized differences that probe into particular model processes and parameterization schemes.

3.4 Cross sections

We would like to wrap up our results in the form of observed and modeled annual zonal mean and longitudinal NO_2 cross sections along the tropics (Figs. 10a, b and 11). Note that in order to bypass pseudoprofile errors, the observed NO_2 pseudoprofiles are scaled in this section by the model profile-to-pseudoprofile ratio as in Eq. (13) to form what is called the observation update.

For the annual zonal mean tropospheric NO_2, the left-to-right panel comparison in Fig. 10a shows that, although the observation update does not change the strength of ma-
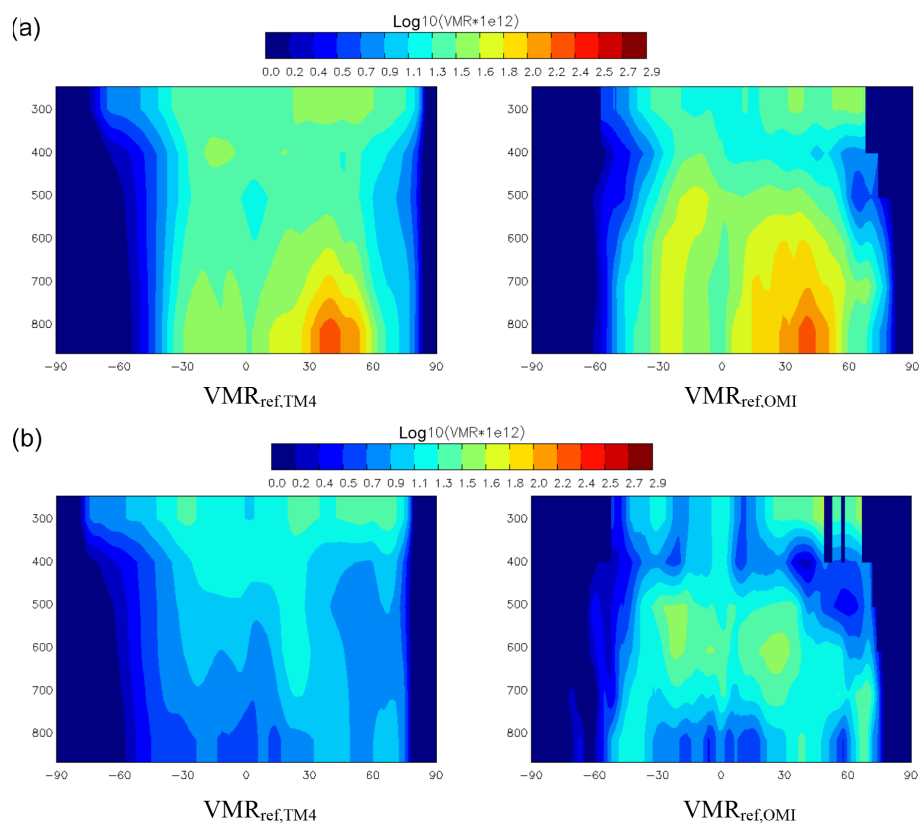
(a)

(b)

Figure 10. (a) Latitude–height cross section of annual zonal mean tropospheric NO_2 VMR in logarithmic scale from TM4 (left) and OMI (right) with CRF > 50 %. **(b)** Same as **(a)** but for the remote Pacific sector (180–135 W).
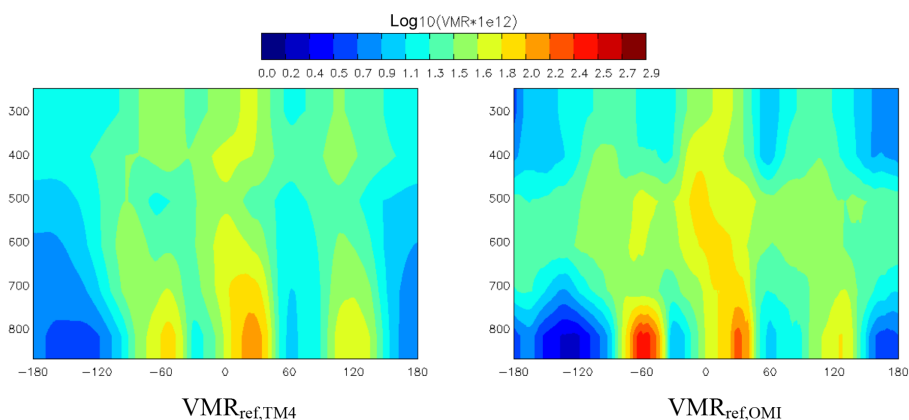

Figure 11. Longitudinal cross section of annual mean tropospheric NO_2 VMR in logarithmic scale from TM4 (left) and OMI (right) with CRF > 50 % over the tropics (10° N–20° S).

jor industrial emission over the northern mid-latitudes at the lowest levels, the associated convective cloud is reaching higher in altitude. In the tropics and southern latitudes, vertical transport of the combination of biomass burning and industrial emissions is stronger and reaching higher – with a prominent high plume originating from the Johannesburg area. The observation update does bring notably

stronger midtropospheric outflows distributed over a broader latitude band and weaker NO_2 signatures at high altitude. The enhanced mid-tropospheric plume is best appreciated in Fig. 10b, which shows the annual zonal mean tropospheric NO_2 averaged over the Pacific Ocean sector (180–135 W) – the dominant sources of NO_2 over the oceans are thought to include the long-range transport from continen-
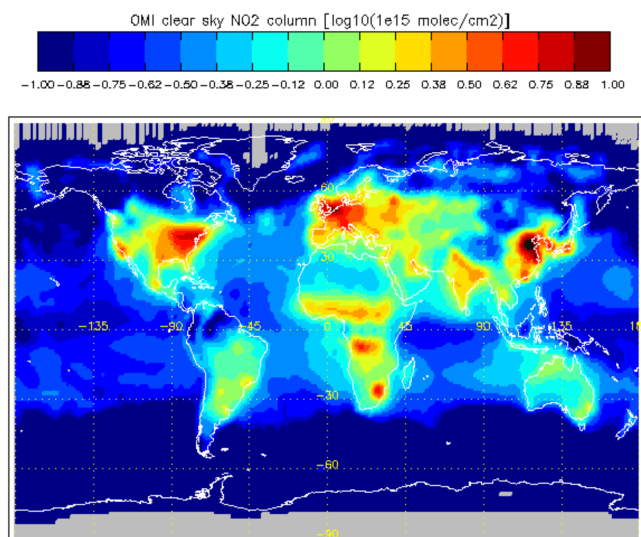
should contribute to the determination of the vertical distribution of lightning NO$_x$, since knowledge of the extent of mixing of air into the cloud as a function of altitude is required to separate the NO$_x$ produced by lightning from that produced by upward transport (Dickerson, 1984).

3.5 Consistency check

Because of the annual and global character of the OMI annual tropospheric NO$_2$ profile climatology estimates, we do not have any direct means to validate them in the same way as has been done, for example, in Choi et al. (2014). But we can check their consistency by demanding that the total tropospheric NO$_2$ column from the cloud-slicing technique does not deviate significantly from the total tropospheric NO$_2$ column observed in clear-sky conditions (see Fig. 12). The total tropospheric NO$_2$ column from the cloud-slicing technique, VCD$_{\text{slicing}}$, is calculated as the sum of partial vertical column densities obtained from the annual mean pseudoprofile VMR as

$$\text{VCD}_{\text{slicing}}(\text{lat}, \text{lon}) = \tag{14}$$

$$\sum_{n=1}^{6} \text{VMR}_i(\text{lat}, \text{lon})(\langle p_{i+1}\rangle - \langle p_i\rangle)/C,$$

where C is the same constant defined in Eq. (8). Note that absent VMR grid values (such as at high altitude over subsidence regions, or at low altitude over the tropical continents) are ignored without provision of a priori information.

We do, however, know that there are some basic differences between NO$_2$ profiles observed under clear and cloudy conditions. In the TM4 model, the differences between cloudy (CRF > 50 %) and clear (CRF < 25 %) profile climatologies (see left panel in Fig. 13 below) show strong negative anomalies over the biomass burning areas (central Africa, southern America, northern Australia, southern India, but also in the Persian Gulf and Turkestan) most likely related to fire suppression during the wet/cloudy season. Over industrial areas (USA, Europe and China) a more complex pattern of anomalies arises that likely results from the competing effects of suppressed photolysis under clouds (small positive anomaly), venting by passing fronts (large negative anomalies) and accumulation patterns dependent on a predominant synoptic weather type (cyclonic or anticyclonic, Pope et al., 2014). This pattern of differences between cloudy and clear annual NO$_2$ profile climatologies is well reproduced by OMI observations (see right panel in Fig. 13 below). The sole difference is that OMI sees larger outflows at higher latitudes in the cloudy case – perhaps a deficiency of the model in redistributing its horizontal flows under frontal conditions.

Another more direct way to perform this consistency check is to look at the differences in total NO$_2$ columns between model (TM4) and observations (OMI) for the clear and cloudy cases separately, as shown in Fig. 14. For the clear-
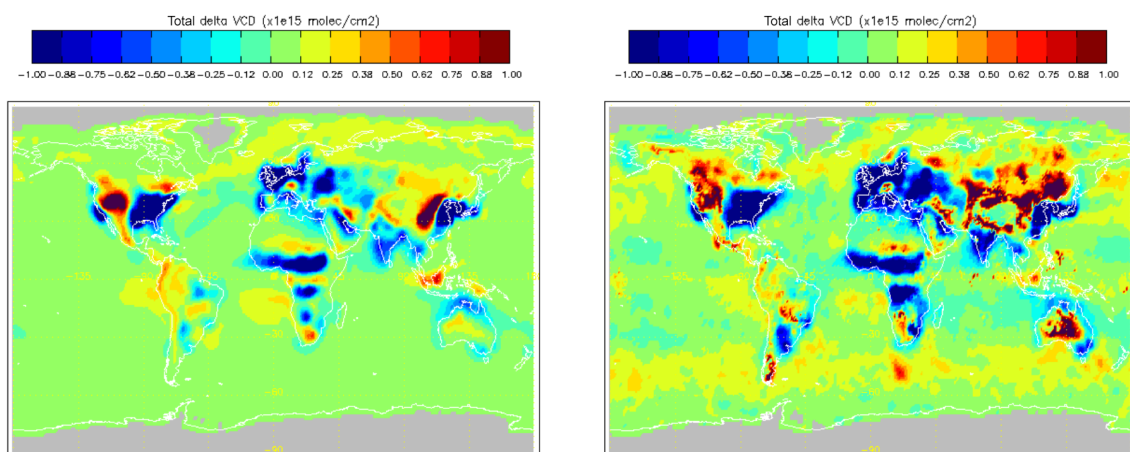

Figure 12. Annual clear-sky OMI tropospheric NO$_2$ total columns in logarithmic scale for the year 2006.

tal source regions, as well as chemical recycling of HNO$_3$ and PAN sources (Staudt et al., 2003). Schultz et al. (1999) actually show that the decomposition of PAN originating from biomass burning actually accounts for most of the mid-tropospheric NO$_x$ in the remote southern Pacific, suggesting that enhanced convective flux from surface sources may not be the only agent responsible for the enhanced mid-tropospheric outflows observed by OMI.

Figure 11 shows a picture for the annual longitudinal NO$_2$ cross section for tropical latitudes between 10° N and 20° S, where the observation update raises the convective plumes from major biomass burning areas in South America, central Africa and Indonesia/northern Australia to higher altitude, between 500 and 600 hPa, with a slight westward tilt and longer downstream transport of cloud outflow at upper levels caused by the tropical easterly jet, and generally weaker NO$_2$ signatures at high altitude.

In summary, the OMI cloud-slicing NO$_2$ profiles seem to suggest that raising the polluted plumes to higher altitudes allows for much longer residence and chemical lifetimes, and longer and more widely distributed horizontal transport of NO$_2$ (following poleward advection and dispersion by the subtropical jet and by baroclinic waves at lower levels) in the mid-troposphere. These observations are in line with reports in Williams et al. (2010) showing that the underestimation of upper tropospheric O$_3$ in TM4 relative to observations over Africa may be linked to a too weak convective uplift using the Tiedtke scheme. The studies of Tost et al. (2007), Barret et al. (2010) and Hoyle et al. (2011) corroborate this finding, indicating that the vertical extent of tropical convection and associated transport of CO and O$_3$ in the middle and upper troposphere is underestimated in Tiedtke-based models. Accurately constraining the convective transport in CTMs

Figure 13. Total tropospheric NO$_2$ columns differences between cloudy (CRF > 50 %) and clear (CRF < 25 %) conditions for TM4 (left) and OMI (right).
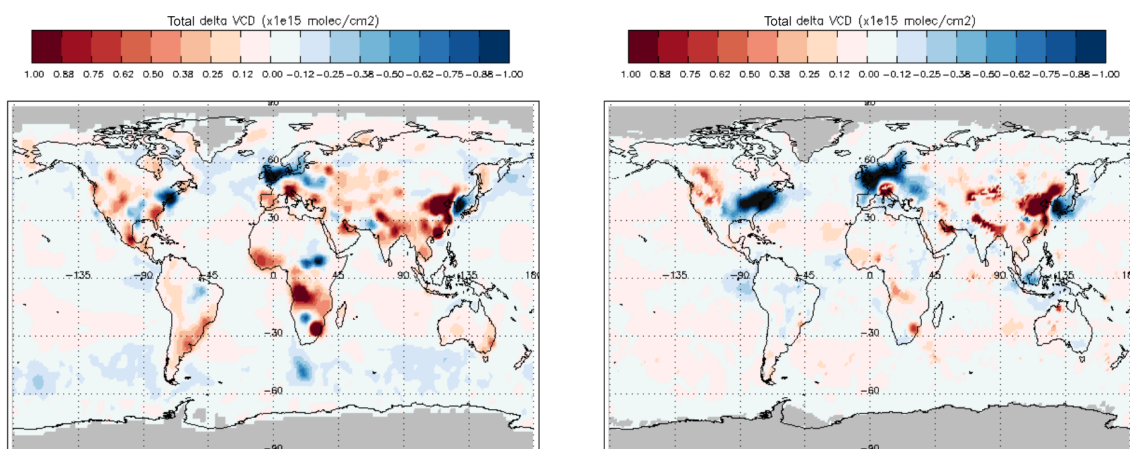

Figure 14. Total tropospheric NO$_2$ column differences (OMI–TM4) in clear (left) and cloudy (right) conditions for the year 2006.

sky case (see left panel in Fig. 14) the pattern of anomalies that arises is consistent with existing long-term satellite NO$_2$ trend studies (van der A et al., 2008; Richter et al., 2005) that report significant reductions in NO$_2$ in Europe and eastern parts of the United States as well as strong increases in China, along with evidence of decreasing NO$_2$ in Japan and increasing NO$_2$ in India, the Middle East, and central Russia – as well as over some spots in the central USA and South Africa. The differences between model and clear-sky OMI NO$_2$ total columns are being used to update the surface emission inventories (Mijling and van der A, 2012; Ding et al., 2015). What is comforting is that a similar pattern of differences arises in the cloudy case (using the cloud-slicing TM4 and OMI profiles), and with a similar amplitude, verifying that the OMI cloud-slicing columns are internally consistent with the clear-sky OMI observations in detecting anomalies that can be ultimately related to outdated model emission inventories.

In Fig. 14, note that the model total tropospheric NO$_2$ columns over clean remote areas (i.e., tropical and extratropical outflow regions over the oceans) in the cloudy case do not deviate in general by more than 0.1×10^{-15} molec cm^{-2} from observations. This is a good result, showing that the estimate of the stratospheric column (by data assimilation) does not produce significant cloud-cover dependent biases in the tropospheric column. If we recall that the observed cloud-slicing NO$_2$ profile over clean remote areas is S-shaped, with a much stronger mid-tropospheric component and a much reduced upper tropospheric load than in the model, then we can infer that there has been as much gain in the mid-tropospheric component as there has been loss at high altitude, which is another form of closure.

3.6 Seasonal analysis

The seasonal mean tropospheric NO$_2$ VMR pseudoprofiles for the DJF, MAM, JJA and SON periods observed by OMI
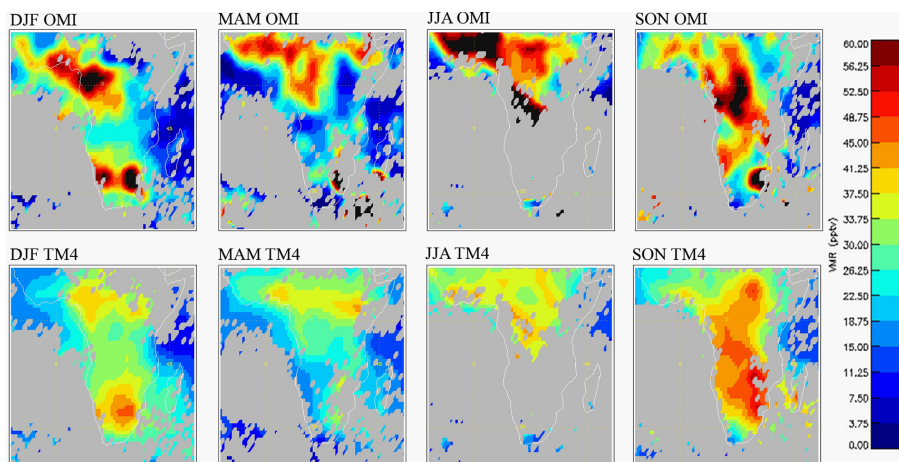
Figure 15. African sector at 280 hPa: seasonal variability in OMI (top row) versus TM4 model (bottom row) average NO$_2$ VMR pseudoprofiles for the year 2006.
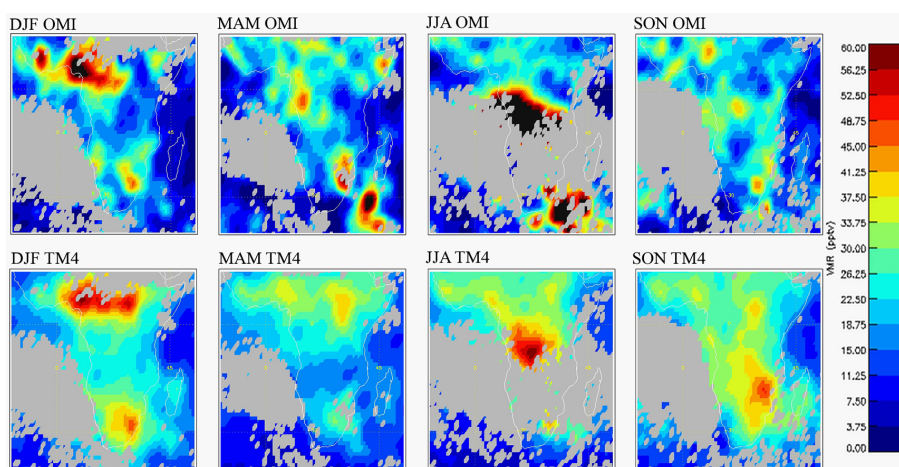

Figure 16. Same as Fig. 15 but at 380 hPa.

over the year 2006 compared against their TM4 model counterparts are shown next. These plots (Figs. 15–33) have been generated using the same cloud-slicing grid and CRF threshold configurations applied for the annual means, with a required minimum of 7 measurements collected per bin during each season (instead of 30 for the annual means). This section is not intended to provide a thorough analysis of seasonal variability in (observed or modeled) tropospheric NO$_2$ profiles but rather to demonstrate the potential of the cloud-slicing technique to provide details that pertain to seasonal as well as to annual means.

The largest signatures of seasonal variability expected to appear in these figures are (a) a seasonal cycle in lightning activity in the upper levels (280–380 hPa) that shifts in latitude following the Sun's declination; (b) a seasonal cycle of biomass burning in the mid-levels (500–620 hPa) basically opposite to that of lightning in case of man-made fires during the dry season, otherwise in phase with lightning;

and (c) a seasonal cycle over industrial areas at lower levels (720–820 hPa), featuring minimum NO$_2$ levels in the summer months due to changes in the lifetime of NO$_x$ (van der A et al., 2008). The seasonal cycle in lightning NO$_x$ emissions may be verified against the climatology of lightning flashes observed by LIS-OTD (data set available online, ftp://ghrc.nsstc.nasa.gov/pub/lis/climatology; see Cecil et al., 2014). The seasonal cycle in biomass burning may be verified against the climatology of ATSR and AVHRR fire counts from Dwyer et al. (2000) and Schultz (2002).

Africa

Over Africa, persistent lightning activity at upper levels is expected to take place about the Equator (the Congo Basin) all year long, shifting southward towards South Africa in SON and DJF, and northward towards the Gulf of Guinea, the Sahel and Sudan in MAM and JJA, features which are all cap-
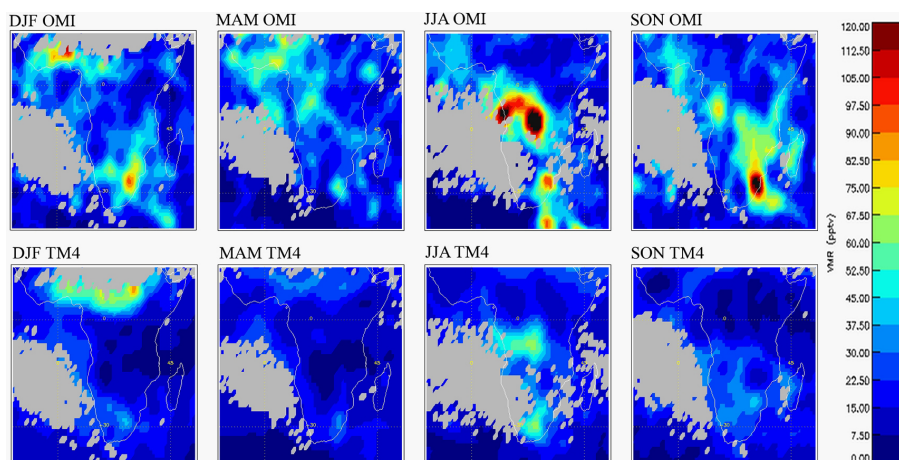
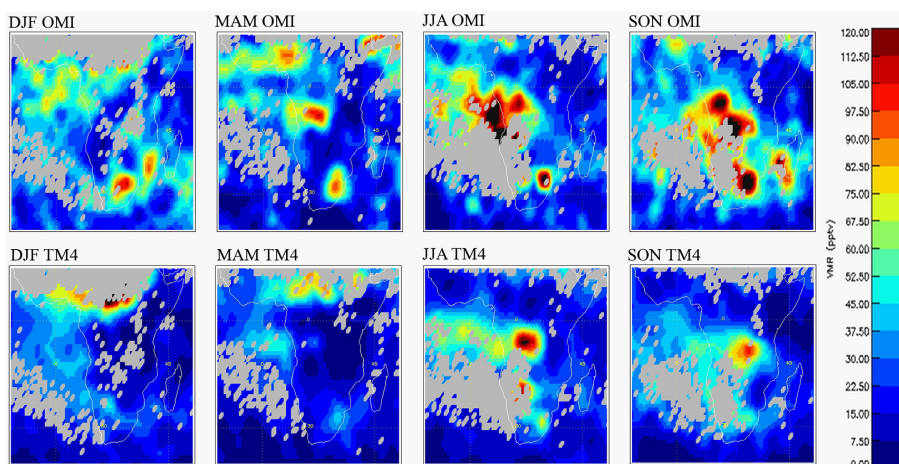**Figure 17.** Same as Fig. 15 but at 500 hPa.

Figure 18. Same as Fig. 15 but at 620 hPa.

tured by OMI in Fig. 15 (in reasonable agreement with TM4, though some discrepancies are apparent too). These lightning signatures are not to be confused with traces of NO$_2$ lifted from biomass burning underneath, which feature a precisely opposite phase. Remarkable biomass burning signatures can be appreciated throughout the entire tropospheric column in Figs. 15–18 as NO$_2$ enhancements north of the Equator (Sahel) in DJF and south of the Equator (Angola and Zambia) in JJA, shifting eastward towards Mozambique and Madagascar in SON (best seen at 500 and 620 hPa in Figs. 17–18). We note that the penetration of seasonal biomass burning signatures into 280–500 hPa is stronger in OMI than in TM4. In addition, note the strong enhancement in lightning activity seen by OMI off the southeast coast of Africa in MAM and JJA at 380 hPa in Fig. 16, in connection with the confluence of the warm Agulhas and the cold Antarctic Circumpolar Current, which is virtually missed by TM4.

South America

Over South America, a maximum in lightning activity is expected to occur over central Brazil in SON, as captured by OMI in Figs. 19–20 (in agreement with TM4, though some discrepancies persist relative to the location of the lightning maximum, as we mentioned when describing the annual means), migrating towards the southeast in DJF. Lightning and precipitation are persistent in the northwest (Colombia, Venezuela and Central America) all year round, intensifying in MAM and JJA, as reasonably captured by OMI in Fig. 19, along with some persistent NO$_2$ enhancements over La Plata Basin and off into the Brazil–Malvinas Confluence Zone. The lightning signatures at upper levels may be partly overlapped by those from biomass burning lifted from underneath, but their separation is more difficult in this case. For instance, the NO$_2$ enhancements detected by OMI at 500 hPa over Brazil in SON and DJF in Fig. 21 correlate well with the lightning signatures at 380 hPa, but they also correlate with
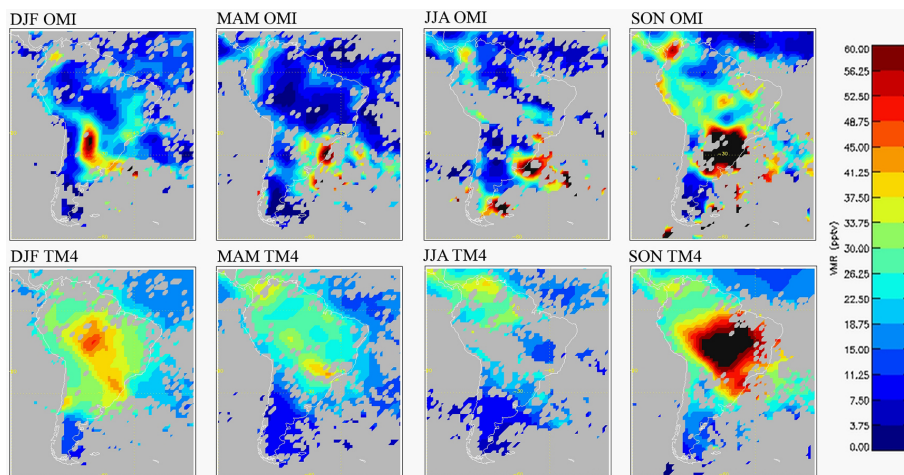
Figure 19. South American sector at 280 hPa: seasonal variability in OMI (top row) versus TM4 model (bottom row) average NO$_2$ VMR pseudoprofiles for the year 2006.
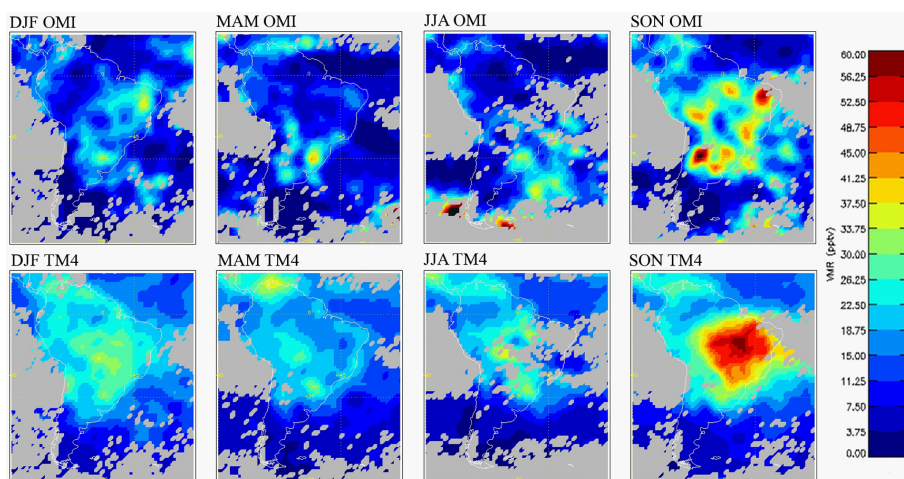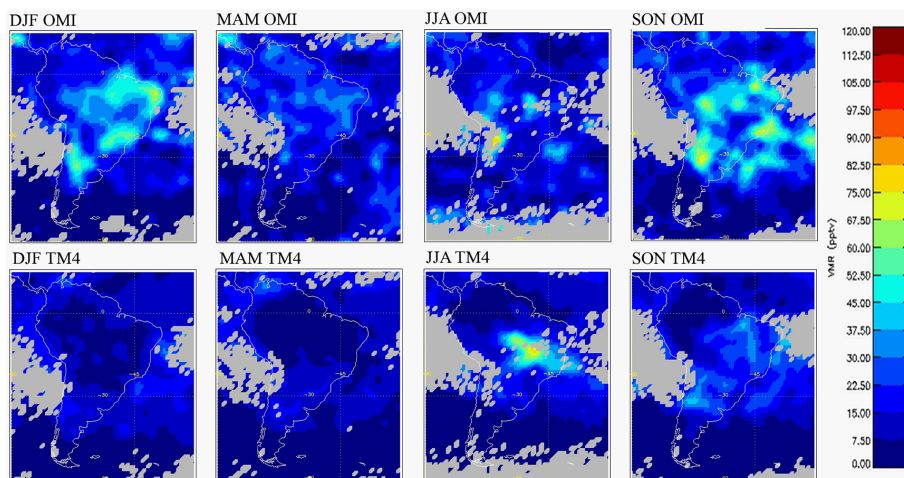

Figure 20. Same as Fig. 19 but at 380 hPa.

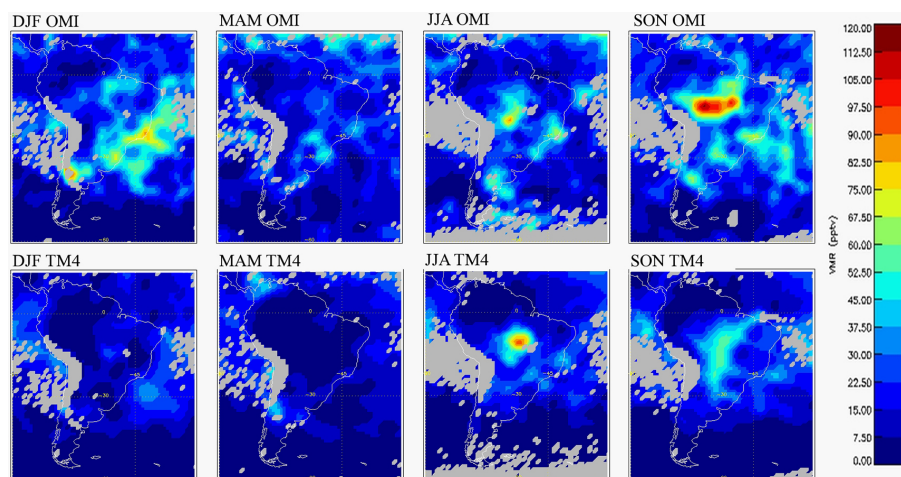**Figure 21.** Same as Fig. 19 but at 500 hPa.

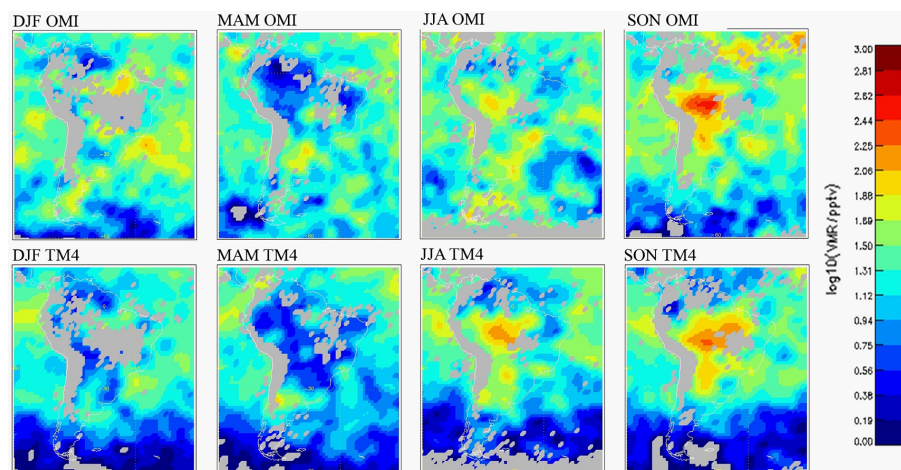**Figure 22.** Same as Fig. 19 but at 620 hPa.

Figure 23. Same as Fig. 19 but at 720 hPa in logarithmic scale.

the biomass burning signals at 620 hPa, indicating that both processes may be occurring at the same time in separate but nearby locations (e.g., combining the start of the wet season in the Amazon Basin in DJF, with the end of the burning season in eastern Brazil). The cycle of biomass burning in South America, which takes place over the dry season, starts in southern Brazil in JJA, finding a maximum in SON eastward towards the coastal states, as OMI captures in Figs. 21–23 (in reasonable agreement with TM4). In DJF, some activity may persist in eastern Brazil and new activity develops over the lower slopes of the Argentinian Andes during the austral summer, generally complicating attribution. Finally, it is interesting to note in Fig. 23 the remarkable decrease in NO$_2$ levels at 720 hPa over the Amazon Basin during the rainy season in DJF and MAM, as if in connection with an efficient NO$_2$ removal mechanism.

Southeast Asia and Australia

At upper levels, one should expect to see some persistent lightning activity over Indonesia all year round, as qualitatively observed by OMI in Fig. 24 (and in agreement with TM4), migrating northward towards South Asia in MAM and JJA, and southward towards Australia in SON and DJF. These lightning signatures may be mixed to greater or lesser degree with NO$_2$ lifted from biomass burning and/or anthropogenic sources underneath. Over South Asia, biomass burning is expected to reach its maximum in MAM, as OMI captures in Figs. 26–28 particularly over northern India and Myanmar. These emissions are likely responsible for a large part of the NO$_2$ enhancement observed around India at upper levels in MAM. The very strong NO$_2$ enhancement observed over South Asia at upper levels in JJA (Figs. 24–25) is very likely related to deep transport of surface emissions (biomass and industrial) during the monsoon season, which
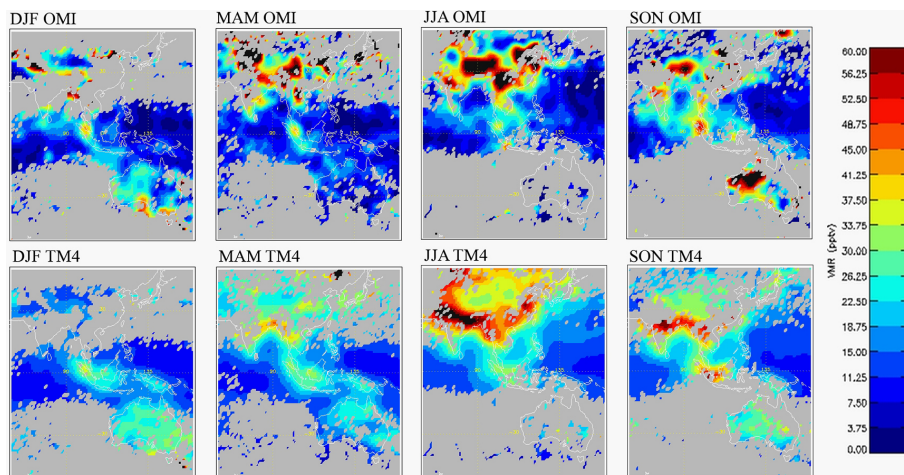
Figure 24. Asian sector at 280 hPa: seasonal variability in OMI (top row) versus TM4 model (bottom row) average NO$_2$ VMR pseudoprofiles for the year 2006.
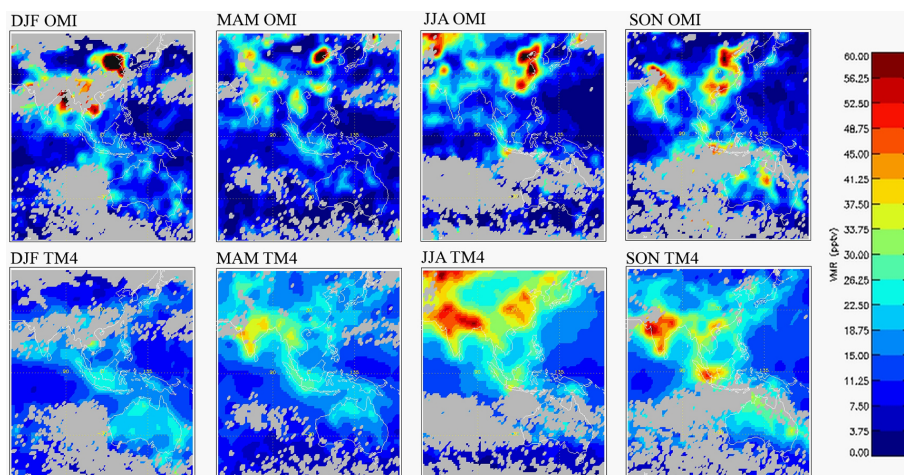

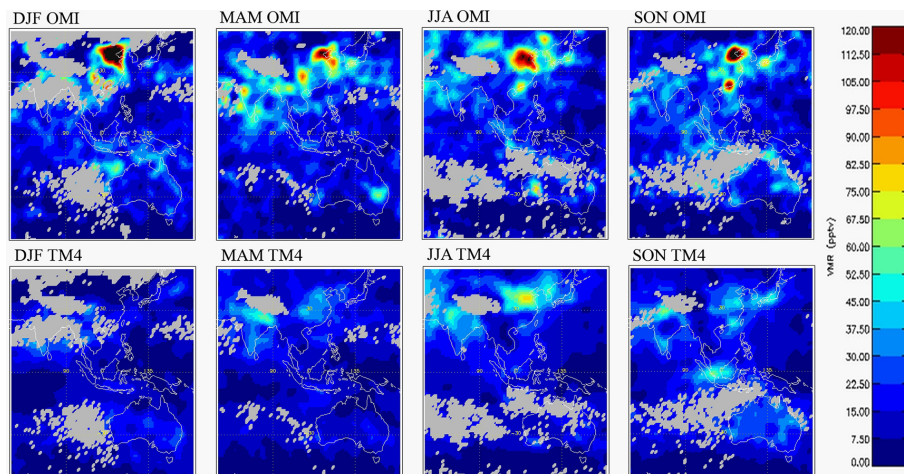
Figure 25. Same as Fig. 24 but at 380 hPa.

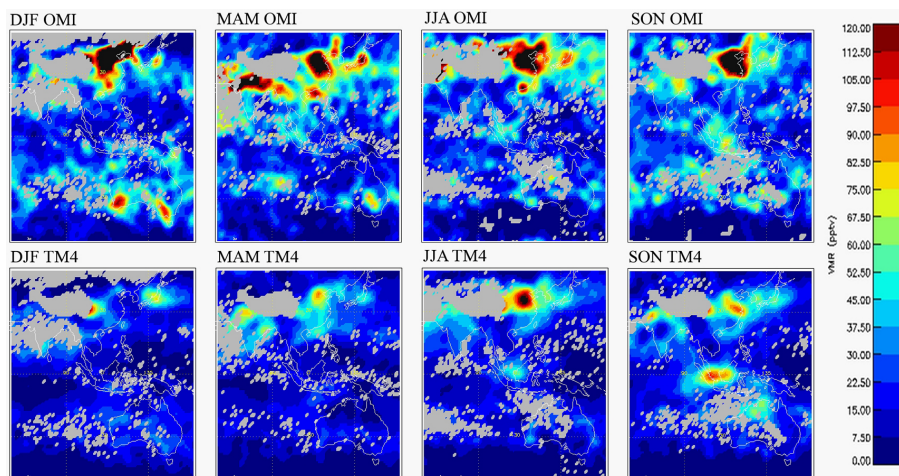**Figure 26.** Same as Fig. 24 but at 500 hPa.

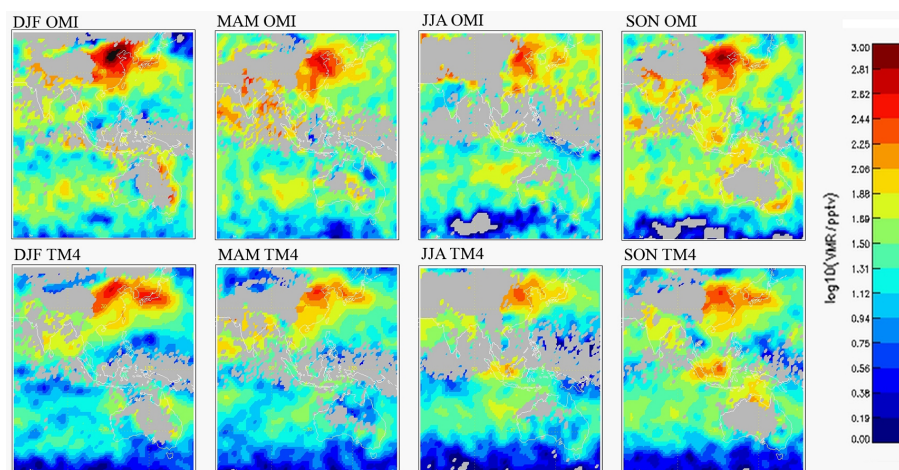**Figure 27.** Same as Fig. 24 but at 620 hPa.

Figure 28. Same as Fig. 24 but at 720 hPa in logarithmic scale.

TM4 locates over the Indo-Gangetic area and OMI locates further east over the Tibetan Plateau. Over Indonesia and northern Australia, a maximum in biomass burning activity is expected be reached in SON, as OMI captures reasonably well in Figs. 26–28, indicating that the strong NO_2 enhancement seen by OMI over northern Australia at 280 hPa in SON may well be tainted by deep transport of biomass burning.

Over a major industrial hub like China, near-surface concentrations of NO_2 around 720–820 hPa are expected to reach minimum/maximum levels in JJA/DJF, just on account of increased/reduced exposure to sunlight (i.e., reduced/increased NO_x lifetime), as shown by both OMI and TM4 in Fig. 28. At mid-tropospheric levels though, other effects such as vertical transport intervene. Note in Figs. 26–27 that the TM4 model registers maximum mid-tropospheric NO_2 levels over China in JJA, and minimum in DJF. However, OMI observes stronger mid-tropospheric NO_2 levels in DJF than in JJA. According to OMI, surface emissions from China (and also from Europe and the USA, as we shall see next) are being transported in larger quantities and to higher altitudes than in the model, particularly during the winter months.

Europe and North America

In connection with summer convection, lightning activity at northern mid-latitudes is expected to be strongest in JJA. Enhancements in upper tropospheric NO_2 are observed by OMI (and TM4) in Fig. 29 over the eastern Mediterranean in JJA and SON. Enhanced NO_2 levels over Siberia in JJA may also be related to summer convection and increased biomass burning. In the USA, lightning activity is expected to reach a maximum in JJA and shift southward towards the Gulf of Mexico in SON and DJF, features which are all registered by OMI in Fig. 29 (in reasonable agreement with TM4, though some discrepancies are apparent in DJF). Figures 30–31 reveal an interesting discrepancy between the OMI and TM4 pseudo-
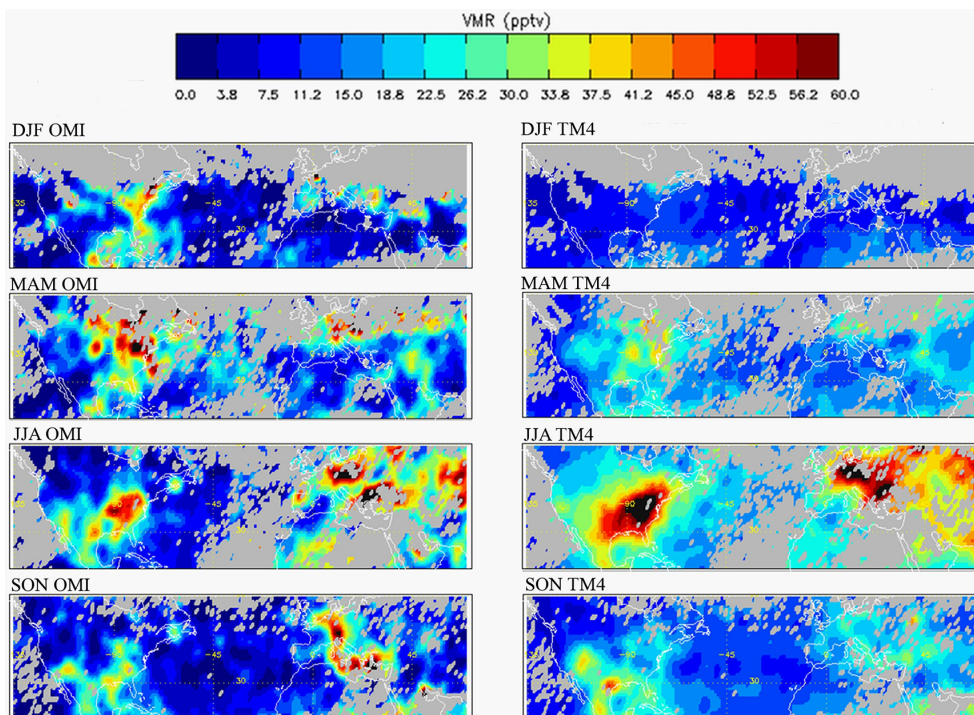
Figure 29. North American and European sectors at 380 hPa: seasonal variability in OMI (left column) versus TM4 model (right column) average NO$_2$ VMR pseudoprofiles for the year 2006.
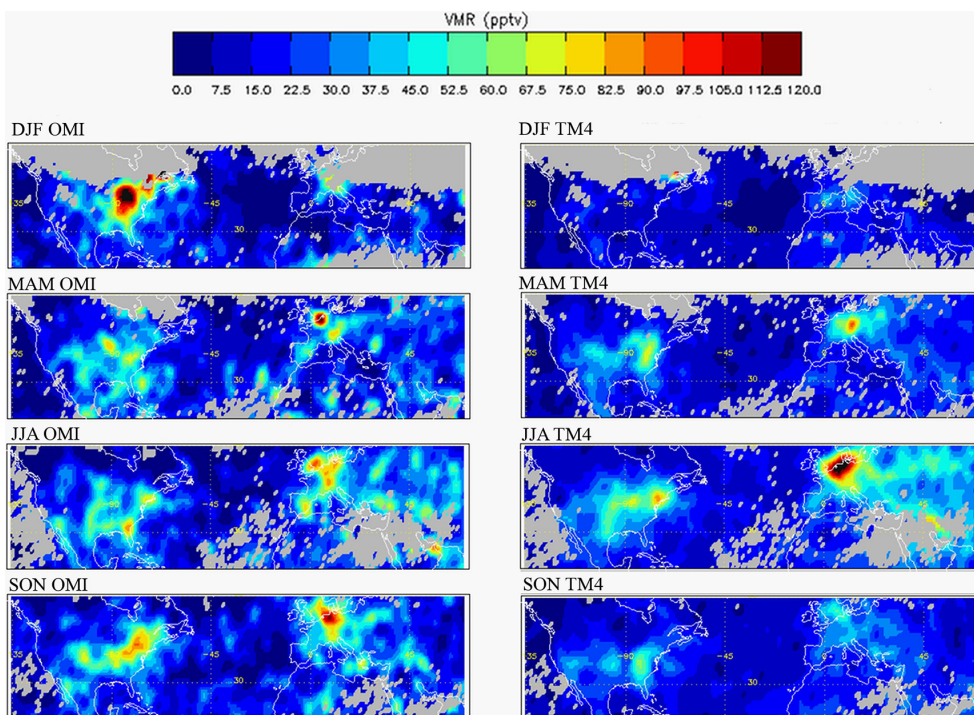

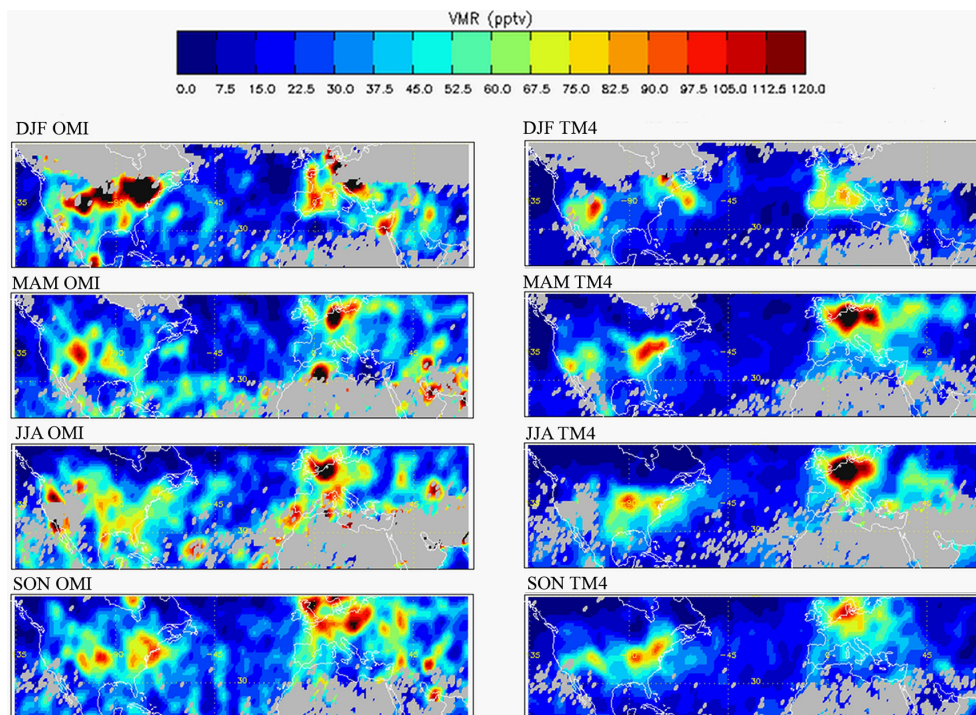**Figure 30.** Same as Fig. 29 but at 500 hPa.

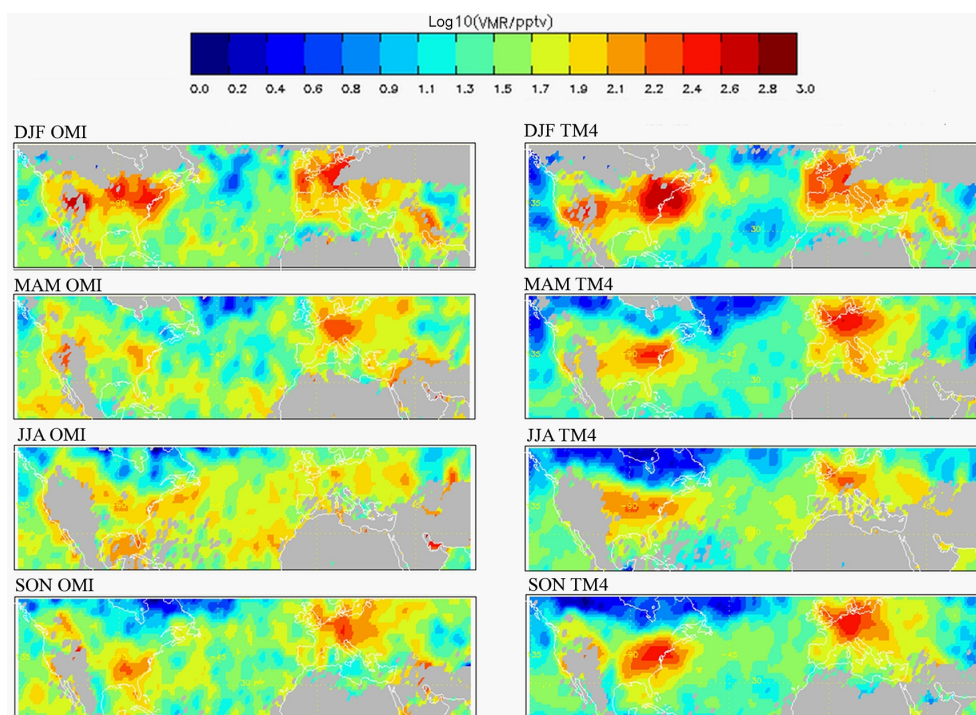**Figure 31.** Same as Fig. 29 but at 620 hPa.

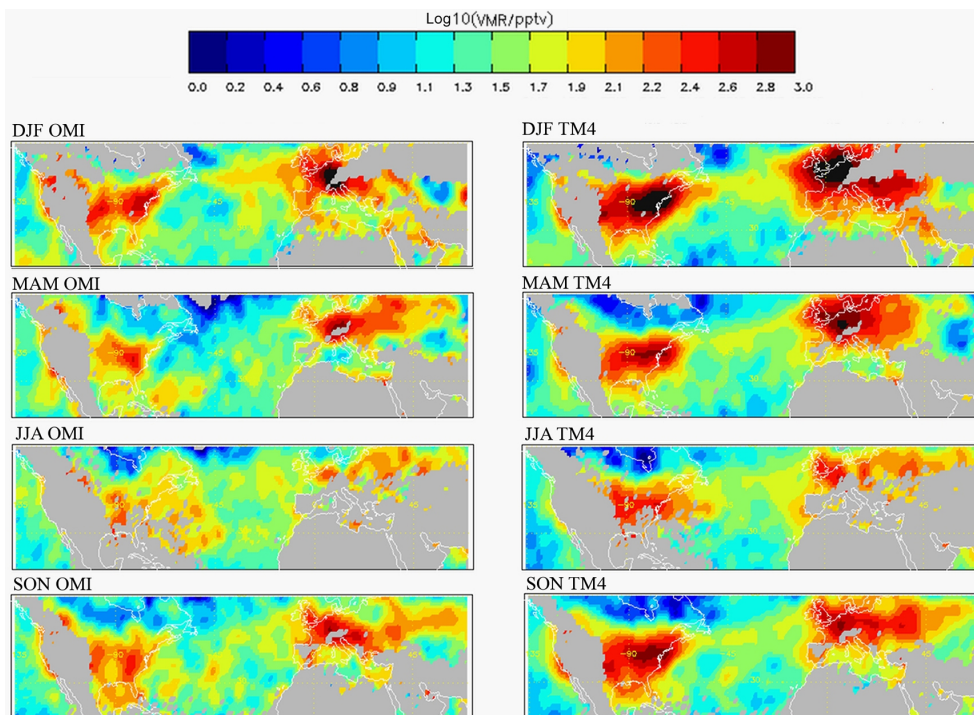**Figure 32.** Same as Fig. 29 but at 720 hPa in logarithmic scale.

Figure 33. Same as Fig. 29 but at 820 hPa in logarithmic scale.

profiles regarding the intensity and reach of convective penetration at 500 hPa of anthropogenic NO$_2$ above major industrial areas. As already noted for China, the TM4 model is placing enhancements of mid-tropospheric NO$_2$ over central Europe and the eastern USA in MAM and JJA, whereas OMI registers a more uniform distribution of mid-tropospheric signatures across the year, showing maxima in DJF and SON. This disagreement is suggestive of problems with the model convective scheme, possibly related to frontal uplift by conveyor belts in the wintertime. At levels closest to the surface, the variation in NO$_2$ concentration over major industrial areas (Europe and the USA, but also China, India and the Middle East) registered by OMI in Figs. 19–20 shows minima in JJA and maxima in DJF, just as expected and in agreement with TM4.

4 Summary and conclusions

In this paper, we derive annual and seasonal global climatologies of tropospheric NO$_2$ profiles from OMI cloudy measurements for the year 2006 using the cloud-slicing method on six pressure levels centered at about 280, 380, 500, 620, 720 and 820 hPa. The cloud-slicing profiles have been estimated after differencing annual and seasonal tropospheric NO$_2$ columns above cloud with respect to pressure, using mean cloud pressures located at about 330, 450, 570, 670, 770 and 870 hPa. We term these objects pseudoprofiles, since the required presence of a probing cloud necessarily draws

the cloud-slicing estimate away from the underlying NO$_2$ profile. The systematic error between the cloud-sliced NO$_2$ pseudoprofile and the actual average NO$_2$ profile in a cloudy atmosphere is called pseudoprofile error, which can be evaluated (and possibly corrected) using a CTM.

The total tropospheric NO$_2$ content in the cloud-slicing profiles is consistent with the OMI clear-sky total tropospheric column for the same year, after making allowance for a natural change in the global NO$_2$ distribution that occurs in passing from clear to cloudy conditions. This change includes suppression of biomass burning during the wet/cloudy season, suppressed NO$_2$ photolysis under clouds, venting by weather fronts and accumulation patterns dependent on the predominant (clear or cloudy sky) synoptic weather type. The internal consistency between OMI clear-sky and cloud-slicing tropospheric NO$_2$ columns confirms the capability of cloud-slicing profiles to detect CTM model anomalies that can be ultimately related to problems in model emission inventories but with additional vertical information that allows distinction between surface, mid-tropospheric and upper-tropospheric processes.

The vertical information contained in OMI tropospheric NO$_2$ profiles derived from the cloud-slicing technique provides a wealth of information that can be used to evaluate global chemistry models and provide guidance in the development of subgrid model parameterizations of convective transport, fire-induced injection, horizontal advective diffusion and lightning NO$_x$ production. Overlapping pro-

cesses (i.e., the effects of deep convection and lightning NO$_x$ in the upper troposphere, the effects of mid-tropospheric convection and anomalies in surface emissions in the mid-troposphere) as well as uncertainties in the chemical degradation and NO$_x$ recycling rates currently limit the degree to which discrepancies between observations and simulations can be unambiguously attributed to a single process, although the availability of observational constraints definitely constitutes an improvement.

To give an example of such an application, we have performed a comparison between cloud-slicing tropospheric NO$_2$ profiles from OMI and the TM4 model. In the upper troposphere (280 and 380 hPa levels), observed NO$_2$ concentration anomalies reveal excessive model background NO$_2$ amounts which are consistent with too strong model lightning emissions over the oceans (and/or too long lifetimes) combined with misplaced lightning NO$_2$ over central Africa and South America, which is indicative of limitations in the convectively driven model lightning NO$_x$ scheme of Meijer et al. (2001). Other anomalies suggest observed enhanced deep transport of NO$_2$ from major industrial centers relative to TM4, including a prominent signal from the Asian summer monsoon plume that the model fails to place accurately, and probable excess model fire-induced convection over Siberia.

In the mid-troposphere (500 and 620 hPa levels), observed NO$_2$ concentration anomalies reveal deficient model background NO$_2$ amounts suggestive of too small model convective inflows into this level, with deficits particularly large over China, the central USA and Europe during the winter months, and the biomass burning regions in central Africa and South America, combined with extensive outflows over the oceans that are stronger and more widely distributed in latitude than in the model. This is consistent with independent reports of underestimation of vertical transport by convective clouds in Tiedtke-based models. Raising the NO$_2$ plumes to higher altitudes allows for much longer residence and chemical lifetimes, and longer and more widely distributed horizontal transport of NO$_2$ following poleward advection and dispersion by the subtropical jet in the mid-troposphere, all of which end up producing typical outflow profiles over the oceans that are generally S-shaped with a prominent mid-tropospheric plume centered at around 620 hPa in the tropics and around 720 hPa in the extratropics. The role that the recycled NO$_x$ component may play in the enhanced mid-tropospheric outflows observed by OMI over remote ocean regions is unclear at this stage, but the cloud-slicing technique shows promise to study such effects.

In the lower troposphere (720 and 820 hPa), observed NO$_2$ concentration anomalies show a pattern that is consistent with deficiencies in model surface emissions related to known NO$_2$ trends characterized by NO$_2$ increases over China, India and the Middle East, and NO$_2$ decreases over the eastern USA, central Europe and Japan. The lower levels also show extensive positive anomalies over the oceans (particularly at 720 hPa), which are indicative of deficient model outflows at low altitudes (and/or too short model lifetimes) with deficient poleward diffusion of NO$_2$ at low to mid-tropospheric levels, and an interesting band of negative anomalies along the ITCZ.

On a seasonal basis, both the OMI and TM4 model pseudoprofiles show seasonal features that are consistent with the available lightning flash and fire count climatologies, and complementary to the results obtained for the annual means. On a finer scale, we observe some significant differences on lightning distribution (at upper levels over Africa and South America, or over the Agulhas and Brazil–Malvinas ocean current confluence zones), and the intensity and reach of convective transport over strong biomass or industrial sources – whose detailed examination deserves future work. For example, we note that the penetration of seasonal biomass burning signatures into 280–500 hPa over Africa is stronger in OMI than in TM4. Also, the penetration of industrial emissions into mid-tropospheric levels over Europe, China and the USA reaches a maximum in MAM and JJA according to TM4, whereas OMI registers a more uniform distribution of mid-tropospheric signatures across the year with maxima in DJF and SON, which is suggestive of problems with the model convective scheme, possibly related to frontal uplift by conveyor belts in the wintertime.

Note that support from a CTM (TM4 in our case) is required to make provision for the cloud-slicing technique in order to determine the a priori corrections for below-cloud leakage, so that a level of trust must initially be placed in the model. When comparing the resulting pseudoprofiles against the a priori information, a number of discrepancies arise which work against our initial trust in the model. This conflicting outcome should be understood and justified to the extent that a priori corrections only have a limited impact on the cloud-slicing profiles. Correcting for pseudoprofile errors using model-based profile-to-pseudoprofile ratios is an entirely different matter. The presence of systematic pseudoprofile error in cloud-slicing estimates and their general predominance over random instrumental error suggest that the vertical information contained in cloudy pixels may be best extracted by an assimilation procedure that updates the atmospheric state (i.e., the model profile shape) at the right time and place using the averaging kernel of the observation. Most data assimilation experiments using OMI NO$_2$ observations have focused to this date on exploiting clear-sky measurements only: our results provide strong motivation to put cloudy pixels to good use as well, as done by, for example, Miyazaki et al. (2014).

Appendix A: Gas columns above and below cloud

If the tropospheric AMF$_{\text{trop}}$ is defined as

$$\text{AMF}_{\text{trop}} = \text{CRF} \cdot \text{AMF}_{\text{cloud}} + (1 - \text{CRF}) \cdot \text{AMF}_{\text{clear}}, \quad \text{(A1)}$$

where the clear AMF can be expressed as

$$
\begin{aligned}
\text{AMF}_{\text{clear}} &= \frac{\sum\limits_{0}^{\text{tropopause}} m_{\text{clear}}(z) n(z)}{\sum\limits_{0}^{\text{tropopause}} n(z)} \quad \text{(A2)} \\[6pt]
&= \frac{\sum\limits_{0}^{\text{CLP}} m_{\text{clear}}(z) \cdot n(z) + \sum\limits_{\text{CLP}}^{\text{tropopause}} m_{\text{clear}}(z) \cdot n(z)}{\sum\limits_{0}^{\text{tropopause}} n(z)} \\[6pt]
&= \frac{\sum\limits_{0}^{\text{CLP}} m_{\text{clear}}(z) \cdot n(z)}{\sum\limits_{0}^{\text{CLP}} n(z)} \cdot \frac{\sum\limits_{0}^{\text{CLP}} n(z)}{\sum\limits_{0}^{\text{trop}} n(z)} \\[6pt]
&\quad + \frac{\sum\limits_{\text{CLP}}^{\text{trop}} m_{\text{clear}}(z) \cdot n(z)}{\sum\limits_{\text{CLP}}^{\text{trop}} n(z)} \cdot \frac{\sum\limits_{\text{CLP}}^{\text{trop}} n(z)}{\sum\limits_{0}^{\text{trop}} n(z)} \\[6pt]
&= \text{AMF}_{\substack{\text{clear} \\ \text{below}}} \cdot \frac{\text{VCD}_{\text{below}}}{\text{VCD}_{\text{trop}}} \\[6pt]
&\quad + \text{AMF}_{\substack{\text{clear} \\ \text{above}}} \cdot \frac{\text{VCD}_{\text{above}}}{\text{VCD}_{\text{trop}}},
\end{aligned}
$$

where m_{clear} is the clear-sky scattering sensitivity and $n(z)$ is the model a priori trace gas profile. Similarly, the cloudy AMF can be expressed as

$$
\begin{aligned}
\text{AMF}_{\text{cloud}} &= \frac{\sum\limits_{0}^{\text{tropopause}} m_{\text{cloud}}(z) \cdot n(z)}{\sum\limits_{0}^{\text{tropopause}} n(z)} \quad \text{(A3)} \\[6pt]
&= \frac{\sum\limits_{0}^{\text{CLP}} m_{\text{cloud}}(z) \cdot n(z) + \sum\limits_{\text{CLP}}^{\text{tropopause}} m_{\text{cloud}}(z) \cdot n(z)}{\sum\limits_{0}^{\text{tropopause}} n(z)} \\[6pt]
&= \frac{\sum\limits_{\text{CLP}}^{\text{trop}} m_{\text{cloud}}(z) \cdot n(z)}{\sum\limits_{\text{CLP}}^{\text{trop}} n(z)} \cdot \frac{\sum\limits_{\text{CLP}}^{\text{trop}} n(z)}{\sum\limits_{0}^{\text{trop}} n(z)} \\[6pt]
&= \text{AMF}_{\substack{\text{cloud} \\ \text{above}}} \cdot \frac{\text{VCD}_{\text{above}}}{\text{VCD}_{\text{trop}}},
\end{aligned}
$$

where m_{cloudy} is the cloudy-sky scattering sensitivity. Note that by construction:

$$\text{VCD}_{\text{trop}} = \sum_{0}^{\text{tropopause}} n(z) = \text{VCD}_{\text{above}} + \text{VCD}_{\text{below}}. \quad \text{(A4)}$$

Then the tropospheric AMF can be written, after inserting Eqs. (A2) and (A3) into Eq. (A1), and rearranging terms relating to above and below components separately, as

$$
\begin{aligned}
\text{AMF}_{\text{trop}} = {} & \quad \text{(A5)} \\[6pt]
& \frac{\text{VCD}_{\text{above}}}{\text{VCD}_{\text{trop}}} \left(\text{CRF} \cdot \text{AMF}_{\substack{\text{cloud} \\ \text{above}}} + (1 - \text{CRF}) \cdot \text{AMF}_{\substack{\text{clear} \\ \text{above}}} \right) \\[6pt]
& + \frac{\text{VCD}_{\text{below}}}{\text{VCD}_{\text{trop}}} (1 - \text{CRF}) \cdot \text{AMF}_{\substack{\text{clear} \\ \text{below}}} \\[6pt]
= {} & \frac{\text{VCD}_{\text{above}}}{\text{VCD}_{\text{trop}}} \text{AMF}_{\text{above}} + \frac{\text{VCD}_{\text{below}}}{\text{VCD}_{\text{trop}}} \text{AMF}_{\text{below}}.
\end{aligned}
$$

From this formulation arise definitions for AMF$_{\text{above}}$ and AMF$_{\text{below}}$:

$$
\begin{aligned}
\text{AMF}_{\text{above}} \equiv {} & \quad \text{(A6)} \\[6pt]
& \frac{\sum\limits_{\text{CLP}}^{\text{trop}} (\text{CRF} \cdot m_{\text{cloud}}(z) + (1 - \text{CRF}) \cdot m_{\text{clear}}(z)) \cdot n(z)}{\sum\limits_{\text{CLP}}^{\text{trop}} n(z)},
\end{aligned}
$$

$$\text{AMF}_{\text{below}} \equiv \frac{\sum\limits_{0}^{\text{CLP}} (1 - \text{CRF}) \cdot m_{\text{clear}}(z) \cdot n(z)}{\sum\limits_{0}^{\text{CLP}} n(z)}. \quad \text{(A7)}$$

Now it is straightforward to write

$$\text{SCD}_{\text{trop}} = \text{AMF}_{\text{trop}} \cdot \text{VCD}_{\text{trop}},$$

which after substitution of Eq. (A5) becomes

$$
\begin{aligned}
\text{SCD}_{\text{trop}} = {} & \quad \text{(A8)} \\[6pt]
& \left(\frac{\text{VCD}_{\text{above}}}{\text{VCD}_{\text{trop}}} \cdot \text{AMF}_{\text{above}} + \frac{\text{VCD}_{\text{below}}}{\text{VCD}_{\text{trop}}} \cdot \text{AMF}_{\text{below}} \right) \text{VCD}_{\text{trop}} \\[6pt]
= {} & \text{VCD}_{\text{above}} \cdot \text{AMF}_{\text{above}} + \text{VCD}_{\text{below}} \cdot \text{AMF}_{\text{below}} \\[6pt]
= {} & \text{SCD}_{\text{above}} + \text{SCD}_{\text{below}}.
\end{aligned}
$$

This allows the separation of the slant column components above and below the cloud in Eq. (A8) as

$$\text{VCD}_{\text{above}} = \frac{(\text{SCD}_{\text{trop}} - \text{SCD}_{\text{below}})}{\text{AMF}_{\text{above}}}. \quad \text{(A9)}$$

Now, in Boersma (2005) the above-cloud part of the NO$_2$ column is retrieved by removing the model predicted ghost

column (integrated from the ground to the cloud level pressure, identical to VCD$_{below}$) that is implicitly added via the tropospheric air mass factor as

$$\text{VCD}_{above} = \text{SCD}_{trop}/\text{AMF}_{trop} - \text{CRF} \cdot \text{VCD}_{below}. \qquad (A10)$$

However, by virtue of Eq. (A4), formulation in Eq. (A10) in Boersma (2005) should be changed to

$$\text{VCD}_{above} = \text{SCD}_{trop}/\text{AMF}_{trop} - \text{VCD}_{below}, \qquad (A11)$$

which is equivalent to Eq. (A9).

References

Acarreta, J. R., De Haan, J. F., and Stammes, P.: Cloud pressure retrieval using the O$_2$-O$_2$ absorption band at 477 nm, J. Geophys. Res., 109, D05204, doi:10.1029/2003JD003915, 2004.

Albrecht, R. I., Naccarato, K. P., Pinto, O., and Pinto, I. R. C. A.: Total Lightning and Precipitation over Brazil: an Overview from 12-Years of TRMM Satellite, AMS Conference, Seattle (WA), 22–27 January 2011, abstract no. 185724, 2011.

Arino, O., Casadio, S., and Serpe, D.: Global night-time fire season timing and fire count trends using the ATSR instrument series, Remote Sens. Environ., 116, 226–238, 2012.

Barret, B., Williams, J. E., Bouarar, I., Yang, X., Josse, B., Law, K., Pham, M., Le Flochmoën, E., Liousse, C., Peuch, V. H., Carver, G. D., Pyle, J. A., Sauvage, B., van Velthoven, P., Schlager, H., Mari, C., and Cammas, J.-P.: Impact of West African Monsoon convective transport and lightning NO$_x$ production upon the upper tropospheric composition: a multi-model study, Atmos. Chem. Phys., 10, 5719–5738, doi:10.5194/acp-10-5719-2010, 2010.

Beirle, S., Spichtinger, N., Stohl, A., Cummins, K. L., Turner, T., Boccippio, D., Cooper, O. R., Wenig, M., Grzegorski, M., Platt, U., and Wagner, T.: Estimating the NOx produced by lightning from GOME and NLDN data: a case study in the Gulf of Mexico, Atmos. Chem. Phys., 6, 1075–1089, doi:10.5194/acp-6-1075-2006, 2006.

Beirle, S., Boersma, F., Platt, U., Lawrence, M. G., and Wagner, T.: Megacity emissions and lifetimes of nitrogen oxides probed from space, Science, 333, 1737–1739, 2011.

Belmonte Rivas, M., Veefkind, P., Boersma, F., Levelt, P., Eskes, H., and Gille, J.: Intercomparison of daytime stratospheric NO$_2$ satellite retrievals and model simulations, Atmos. Meas. Tech., 7, 2203–2225, doi:10.5194/amt-7-2203-2014, 2014.

Boersma, F., Eskes, H., and Brinskma, E.: Error analysis for tropospheric NO$_2$ retrieval from space, J. Geophys. Res., 109, D04311, doi:10.1029/2003JD003962, 2004.

Boersma, K. F., Eskes, H. J., Meijer, E. W., and Kelder, H. M.: Estimates of lightning NOx production from GOME satellite observations, Atmos. Chem. Phys., 5, 2311–2331, doi:10.5194/acp-5-2311-2005, 2005.

Boersma, K. F., Eskes, H. J., Veefkind, J. P., Brinksma, E. J., van der A, R. J., Sneep, M., van den Oord, G. H. J., Levelt, P. F., Stammes, P., Gleason, J. F., and Bucsela, E. J.: Near-real time retrieval of tropospheric NO$_2$ from OMI, Atmos. Chem. Phys., 7, 2103–2118, doi:10.5194/acp-7-2103-2007, 2007.

Boersma, K. F., Eskes, H. J., Dirksen, R. J., van der A, R. J., Veefkind, J. P., Stammes, P., Huijnen, V., Kleipool, Q. L., Sneep, M., Claas, J., Leitão, J., Richter, A., Zhou, Y., and Brunner, D.: An improved tropospheric NO2 column retrieval algorithm for the Ozone Monitoring Instrument, Atmos. Meas. Tech., 4, 1905–1928, doi:10.5194/amt-4-1905-2011, 2011.

Boersma, K. F., Vinken, G. C. M., and Eskes, H. J.: Representativeness errors in comparing chemistry transport and chemistry climate models with satellite UV/Vis tropospheric column retrievals, Geosci. Model Dev. Discuss., 8, 7821–7877, doi:10.5194/gmdd-8-7821-2015, 2015.

Boucher, O., Randall, D., Artaxo, P., Bretherton, C., Feingold, G., Forster, P., Kerminen, V.-M., Kondo, Y., Liao, H., Lohmann, U., Rasch, P., Satheesh, S. K., Sherwood, S., Stevens, B., and Zhang, X. Y.: Clouds and aerosols, in: Climate Change 2013: The Physical Science Basis. Contribution of Working Group I to the Fifth Assessment Report of the Intergovernmental Panel on Climate Change, edited by: Stocker, T. F., Qin, D., Plattner, G.-K., Tignor, M., Allen, S. K., Boschung, J., Nauels, A., Xia, Y., Bex, V., and Midgley, P. M., Cambridge University Press, Cambridge, UK and New York, NY, USA, 571–658, 2013.

Cecil, D. J., Buechler, D. E., and Blakeslee, R. J.: Gridded lightning climatology from TRMM-LIS and OTD: dataset description, Atmos. Res., 135–136, 404–414, 2014.

Choi, S., Joiner, J., Choi, Y., Duncan, B. N., Vasilkov, A., Krotkov, N., and Bucsela, E.: First estimates of global free-tropospheric NO$_2$ abundances derived using a cloud-slicing technique applied to satellite observations from the Aura Ozone Monitoring Instrument (OMI), Atmos. Chem. Phys., 14, 10565–10588, doi:10.5194/acp-14-10565-2014, 2014.

Dickerson, R. R.: Measurements of reactive nitrogen compounds in the free troposphere, Atmos. Environ., 18, 2585–2593, 1984.

Ding, J., van der A, R. J., Mijling, B., Levelt, P. F., and Hao, N.: NOx emission estimates during the 2014 Youth Olympic Games in Nanjing, Atmos. Chem. Phys., 15, 9399–9412, doi:10.5194/acp-15-9399-2015, 2015.

Dwyer, N., Pinnock, S., Gregoire, J.-M., and Pereira, J. M. C.: Global spatial and temporal distribution of vegetation fire as determined from satellite observations, Int. J. Rem. Sens., 21, 1289–1302, doi:10.1080/014311600210182, 2000.

Folkins, I., Bernath, P., Boone, C., Donner, L. J., Eldering, A., Lesins, G., Martin, R. V., Sinnhuber, B. M., and Walker, K.: Testing convective parameterizations with tropical measurements of HNO$_3$, CO, H$_2$O and O$_3$: implications for the water vapor budget, J. Geophys. Res., 111, D23304, doi:10.1029/2006JD007325, 2006.

Houweling, S., Dentener, F. J., and Lelieveld, J.: The impact of non-methane hydrocarbon compounds on tropospheric chemistry, J. Geophys. Res., 103, 10673–10696, 1998.

Hoyle, C. R., Maréçal, V., Russo, M. R., Allen, G., Arteta, J., Chemel, C., Chipperfield, M. P., D'Amato, F., Dessens, O., Feng, W., Hamilton, J. F., Harris, N. R. P., Hosking, J. S., Lewis, A. C., Morgenstern, O., Peter, T., Pyle, J. A., Reddmann, T., Richards, N. A. D., Telford, P. J., Tian, W., Viciani, S., Volz-Thomas, A., Wild, O., Yang, X., and Zeng, G.: Representation of tropical deep convection in atmospheric models – Part 2: Tracer transport, Atmos. Chem. Phys., 11, 8103–8131, doi:10.5194/acp-11-8103-2011, 2011.

Huijnen, V., Flemming, J., Kaiser, J. W., Inness, A., Leitão, J., Heil, A., Eskes, H. J., Schultz, M. G., Benedetti, A., Hadji-Lazaro, J., Dufour, G., and Eremenko, M.: Hindcast experiments of tropo-

spheric composition during the summer 2010 fires over western Russia, Atmos. Chem. Phys., 12, 4341–4364, doi:10.5194/acp-12-4341-2012, 2012.

Jakob, C.: An improved strategy for the evaluation of cloud parameterizations in GCMs, B. Am. Meteorol. Soc., 84, 1387–1401, doi:10.1175/BAMS-84-10-1387, 2003.

Kar, J., Bremer, H., Drummond, J. R., Rochon, Y. J., Jones, D. B., Nichitiu, F., Zou, J., Liu, J., Gille, J., Edwards, D. P., Deeter, M., Francis, G., Ziskin, D., and Warner, J.: Evidence of vertical transport of carbon monoxide from MOPITT, Geophys. Res. Lett., 31, L23105, doi:10.1029/2004GL021128, 2004.

Krol, M. C. and van Weele, M.: Implications of variations in photodissociation rates for global tropospheric chemistry, Atmos. Environ., 31, 1257–1273, 1997.

Landgraf, J. and Crutzen, P. J.: An efficient method for online calculations of photolysis and heating rates, J. Atmos. Sci., 55, 863–878, 1998.

Levelt, P. F., van den Oord, G., Dobber, M. R., Malkki, A., Visser, H., de Vries, J., Stammes, P., Lundell, J., and Saari, H.: The Ozone Monitoring Instrument, IEEE T. Geosci. Remote, 44, 1093–1101, 2006.

Liu, C., Beirle, S., Butler, T., Hoor, P., Frankenberg, C., Jöckel, P., Penning de Vries, M., Platt, U., Pozzer, A., Lawrence, M. G., Lelieveld, J., Tost, H., and Wagner, T.: Profile information on CO from SCIAMACHY observations using cloud slicing and comparison with model simulations, Atmos. Chem. Phys., 14, 1717–1732, doi:10.5194/acp-14-1717-2014, 2014.

Mahowald, N. M., Rasch, P. J., and Prinn, R. G.: Cumulus parameterization in chemical transport models, J. Geophys. Res., 100, 26173–26189, 1995.

Martin, R. V., Jacob, D. J., Chance, K., Kurosu, T. P., Palmer, P. I., and Evans, M. J.: Global inventory of nitrogen oxide emissions constrained by space-based observations of NO$_2$ columns, J. Geophys. Res., 108, 4537, doi:10.1029/2003JD003453, 2003.

Martin, R. V., Sauvage, B., Folkins, I., Sioris, C.E, Boone, C., Bernath, P., and Ziemke, J.: Space-based constraints on the production of nitric oxide by lightning, J. Geophys. Res., 112, D09309, doi:10.1029/2006JD007831, 2007.

Meijer, E. W., Velthoven, P. F. J., Brunner, D. W., Huntrieser, H., and Kelder, H.: Improvement and evaluation of the parameterisation of nitrogen oxide production by lightning, Phys. Chem. Earth, 26, 557–583, 2001.

Mijling, B. and van der A, R. J.: Using daily satellite observations to estimate emissions of short lived air pollutants on a mesoscopic scale, J. Geophys. Res., 117, D17302, doi:10.1029/2012JD017817, 2012.

Miyazaki, K., Eskes, H. J., and Sudo, K.: Global NOx emission estimates derived from an assimilation of OMI tropospheric NO2 columns, Atmos. Chem. Phys., 12, 2263–2288, doi:10.5194/acp-12-2263-2012, 2012.

Miyazaki, K., Eskes, H. J., Sudo, K., and Zhang, C.: Global lightning NOx production estimated by an assimilation of multiple satellite data sets, Atmos. Chem. Phys., 14, 3277–3305, doi:10.5194/acp-14-3277-2014, 2014.

Murray, L. T., Jacob, D. J., Logan, J., Hudman, R., and Koshak, W. J.: Optimized regional and interannual variability of lightning in a global chemical transport model constrained by LIS-OTD satellite data, J. Geophys. Res., 117, D20307, doi:10.1029/2012JD017934, 2012.

Nam, C., Quaas, J., Neggers, R., Siegenthaler-Le Drian, C., and Isotta, F.: Evaluation of boundary layer cloud parameterizations in the ECHAM5 general circulation model using CALIPSO and CloudSAT satellite data, J. Adv. Model. Earth Syst., 6, 300–314, doi:10.1002/2013MS000277, 2014.

Olivier, J., Peters, J., Granier, C., Petron, G., Müller, J. F., and Wallens, S.: Present and Future Emissions of Atmospheric Compounds, POET report #2, EU report EV K2-1999-00011, available at: http://tropo.aeronomie.be/pdf/POET_emissions_report.pdf, 2003.

Pickering, K. E., Thompson, A. M., Dickerson, R. R., Luke, W. T., and McNamara, D. P.: Free tropospheric ozone production following entrainment of urban plumes into deep convection, J. Geophys. Res., 97, 17985–18000, 1992.

Pickering, K. E., Wang, Y., Tao, W. K., Price, C., and Muller, F.: Vertical distributions of lightning NO$_x$ for use in regional and global chemical transport models, J. Geophys. Res., 103, 31203–31216, 1998.

Pope, R. J., Savage, N. H., Chipperfield, M. P., Arnold, S. R., and Osborn, T. J.: The influence of synoptic weather regimes on UK air quality: analysis of satellite column NO$_2$, Atmos. Sci. Lett., 15, 211–217, 2014.

Richter, A., Burrows, J. P., Nuss, H., Granier, C., and Niemeier, U.: Increase in tropospheric nitrogen dioxide over Chine observed from space, Nature, 437, 129–132, 2005.

Russell, G. L. and Lerner, J. A.: A new finite differencing scheme for the tracer transport equation, J. Appl. Meteorol., 20, 1483–1498, 1981.

Schumann, U. and Huntrieser, H.: The global lightning-induced nitrogen oxides source, Atmos. Chem. Phys., 7, 3823-3907, doi:10.5194/acp-7-3823-2007, 2007.

Schultz, M., Jacob, D.J., Wang, Y., Logan, J. A., Atlas, E. L., Blake, D. R., Blake, N. J., Bradshaw, J. D., Browell, E. V., Fenn, M. A., Flocke, F., Gregory, G. L., Heikes, B. G., Sachse, G. W., Sandholms, S. T., Shetter, R. E., Singh, H. B., and Talbot, R. W.: On the origin of tropospheric ozone and NO$_x$ over the tropical south Pacific, J. Geophys. Res., 104, 5829–5844, 1999.

Schultz, M. G.: On the use of ATSR fire count data to estimate the seasonal and interannual variability of vegetation fire emissions, Atmos. Chem. Phys., 2, 387–395, doi:10.5194/acp-2-387-2002, 2002.

Sneep, M., de Haan, J. F., Stammes, P., Wang, P., Vanbauce, C., Joiner, J., Vasilkov, A. P., and Levelt, P. F.: Three way comparison between OMI and PARASOL cloud pressure products, J. Geophys. Res., 113, D15S23, doi:10.1029/2007JD008694, 2008.

Stammes, P., Sneep, M., de Haan, J. F., Veefkind, J. P., Wang, P., and Levelt, P. F.: Effective cloud fraction from the Ozone Monitoring Instrument: theoretical framework and validation, J. Geophys. Res., 113, D15S23, doi:10.1029/2007JD008820, 2008.

Staudt, A. C., Jacob, D. J., Ravetta, F., Logan, J. A., Bachiochi, D., Krishnamurti, T. N., Sandholm, S., Ridley, B., Singh, H. B., and Talbot, B.: Sources and chemistry of nitrogen oxides over the tropical Pacific, J. Geophys. Res., 108, 8239, doi:10.1029/2002JD002139, 2003.

Tiedtke, M.: A comprehensive mass flux scheme for cumulus parameterization in large-scale models, Mon. Weather Rev., 117, 1779–1800, 1989.

Tie, X., Madronich, S., Waters, S., Zhang, R., Rasch, P., and Collins, W.: Effects of clouds on photolysis and oxidants in the troposphere, J. Geophys. Res., 108, 4642, doi:10.1029/2003JD003659, 2003.

Tost, H., Jöckel, P., and Lelieveld, J.: Lightning and convection parameterisations –uncertainties in global modelling, Atmos. Chem. Phys., 7, 4553–4568, doi:10.5194/acp-7-4553-2007, 2007.

van der A, R. J., Eskes, H., Boesma, K. F., Noije, T. P. C., Roozendael, M., Smedt, I., Peters, D. H. M. U., and Meijer, E. W.: Trends, seasonal variability and dominant NO$_x$ sources derived from a ten year records of NO$_2$ measured from space, J. Geophys. Res., 113, D04302, doi:10.1029/2007JD009021, 2008.

Williams, J. E., Scheele, R., Velthoven, P., Bouarar, I., Law, K., Josse, B., Peuch, V. H., Yang, X., Pyle, J., Thouret, V., Barret, B., Liousse, C., Hourdin, F., Szopa, S., and Cozic, A.: Global chemistry simulations in the AMMA (African Monsoon Multidisciplinary Analysis) multimodel intercomparison project, B. Am. Meteorol. Soc., 91, 5, 612–624, 2010.

Ziemke, J. R., Chandra, S., and Barthia, P. K.: Cloud slicing: a new technique to derive upper tropospheric ozone from satellite measurements, J. Geophys. Res., 106, 9853–9867, 2001.